International Journal of Biological Macromolecules 239 (2023) 124276

Contents lists available at ScienceDirect

International Journal of Biological Macromolecules

journal homepage: www.elsevier.com/locate/ijbiomac

Sustainable soy protein microsponges for efficient removal of lead (II) from aqueous environments

Sara Anselmo [a,1], Tiziana Avola [b,1], Kleopatra Kalouta [c,d], Salvatore Cataldo [a], Giuseppe Sancataldo [a], Nicola Muratore [a], Vito Foderà [d], Valeria Vetri [a,*], Alberto Pettignano [a,*]

[a] Dipartimento di Fisica e Chimica – Emilio Segrè, Università di Palermo, Viale delle Scienze, I-90128 Palermo, Italy
[b] Dipartimento di Chimica, Università di Milano, via Golgi 19, I-20133 Milano, Italy
[c] Dipartimento di Scienze e Tecnologie Biologiche Chimiche e Farmaceutiche (SteBiCeF), Università di Palermo, Viale delle Scienze, I-90128 Palermo, Italy
[d] Department of Pharmacy, University of Copenhagen, Universitetsparken 2, 2100 Copenhagen, Denmark

ARTICLE INFO

Keywords:
Lead
Soy
Amyloid superstructures
Adsorption
Green chemistry
Water contamination

ABSTRACT

Protein-based materials recently emerged as good candidates for water cleaning applications, due to the large availability of the constituent material, their biocompatibility and the ease of preparation. In this work, new adsorbent biomaterials were created from Soy Protein Isolate (SPI) in aqueous solution using a simple environmentally friendly procedure. Protein microsponge-like structures were produced and characterized by means of spectroscopy and fluorescence microscopy methods. The efficiency of these structures in removing Pb^{2+} ions from aqueous solutions was evaluated by investigating the adsorption mechanisms. The molecular structure and, consequently, the physico-chemical properties of these aggregates can be readily tuned by selecting the pH of the solution during production. In particular, the presence of β-structures typical of amyloids as well as an environment characterized by a lower dielectric constant seem to enhance metal binding affinity revealing that hydrophobicity and water accessibility of the material are key features affecting the adsorption efficiency. Presented results provide new knowledge on how raw plant proteins can be valorised for the production of new biomaterials. This may offer extraordinary opportunities towards the design and production of new tailorable biosorbents which can also be exploited for several cycles of purification with minimal reduction in performance.
Synopsis: Innovative, sustainable plant-protein biomaterials with tunable properties are presented as green solution for water purification from lead(II) and the structure-function relationship is discussed.

1. Introduction

Contamination of aquatic systems is a serious environmental issue causing diseases and death for people, plants and living organisms worldwide. A principal source of water pollution is the industry, which releases increasing amounts of toxic pollutants in the environment, including heavy metals. The latter are eco-toxicological hazards, they do not degrade and they accumulate in vital organs of humans and animals causing irreversible damages [1–3].

In order to improve environmental sustainability, rational and efficient wastewater management is needed and water must be purified at the level of being safe for drinking, washing, and for being released into rivers, lakes and the sea [4]. Currently, various technologies exist for water purification [5] such as sorption [6–9], chemical precipitation [10], ion exchange [11], reverse osmosis [12] and electrochemical treatments [13]. Among those, sorption emerges as a promising solution due to its high efficiency, low-cost, and ease of operation [14–16]; for these reasons, research is ongoing for new biocompatible sorbent materials.

Several kinds of natural sorbent materials such as fungi [17], algae [18], bacteria [19] and by-products from industrial processes [20] are currently under the lens of scientists for their potential low environmental impact. Moreover, polymeric adsorbents, which have shown a high removal capability of heavy metal ions from wastewater [21], have been tested. Biopolymers, such as cellulose, calcium alginate, pectate, polygalacturonate and starch have shown interesting properties as adsorbents for water treatment due to their biodegradability [22–24]. In this context, proteins are emerging as promising eco-compatible binding

* Corresponding authors.
E-mail addresses: valeria.vetri@unipa.it (V. Vetri), alberto.pettignano@unipa.it (A. Pettignano).
[1] These authors equally contributed to the present work.

https://doi.org/10.1016/j.ijbiomac.2023.124276
Received 13 January 2023; Received in revised form 17 March 2023; Accepted 28 March 2023
Available online 1 April 2023
0141-8130/© 2023 The Authors. Published by Elsevier B.V. This is an open access article under the CC BY license (http://creativecommons.org/licenses/by/4.0/).

blocks for the production of new green adsorbers, containing functional groups with metal-binding capability [14,25,26]. Side chains of cysteine, aspartic acid, glutamic acid, and histidine are the most favored motifs to coordinate heavy metals [27].

The possibility to induce supramolecular association of protein molecules and to tailor the structural properties of newly formed bidimensional or tridimensional structures, at molecular level, paves the way for the design of tailored materials for different applications [28]. A plethora of structures such as fibrils, spherical condensates and gels, can be generated with sizes ranging from the nano to the macroscopic scale. The structures of these bidimensional or tridimensional supramolecular assemblies as well as their mechanical properties, charge, polarity, water accessibility and stability can be tuned by regulating the growth conditions [29–32]. In particular, amyloid fibrils have shown good capability to remove heavy metals and other water pollutants from water, this property being also attributed to the presence of a high content of intermolecular β-structures, which are considered to be an essential feature for water purification properties [26,33–35].

In a previous work [25], we have demonstrated the excellent Pb^{2+} ions adsorption efficiency of Bovine Serum Albumin (BSA) micro-sized amyloid-like spherical particles. A complex adsorption mechanism was highlighted, resulting from the balance between specific interactions with functional groups in protein structure and heterogeneous interactions common to polypeptide chains. These features were related to the amyloid state and modifications of the hydration layer of protein microparticles [25].

In the present work, we generate a material based on a renewable building block, Soy Protein Isolate (SPI), by using green chemistry principles. SPI is a plant-based extract from the soybean oil production industry, which emerges as a good candidate for new functional, multipurpose materials, being green, intrinsically biocompatible, biodegradable, abundant in nature and cost-effective [36–38].

The trimer, glycoprotein β-conglycinin (7S) and the hexamer glycinin (11S) are the two major protein fractions in SPI [39] the isoelectric point of which is reported to be in the pH 4–5 interval [40].

Soy protein in combination with polymers was previously used to create hybrid materials for water purification [41], including microspheres or hydrogels [14,42].

Here, we show the possibility of obtaining SPI microsponges with amyloid-like molecular structures by simply incubating SPI aqueous solutions at high temperature and at two different pHs, namely pH 5 and pH 9, which are close and away from the isoelectric point of SPI, respectively. This in the light of the idea that, in addition to the binding sites intrinsically present in proteins such as hydroxyl, amino, and other active functional groups [27], the three-dimensional structure of microsponges could benefit from porosity (which makes them solvent-accessible), large surface area and open-hole structure for metal adsorption.

The rationale of this study lies on the well supported hypothesis that by modulating solution conditions it is possible to control the structure and physicochemical properties of protein aggregates [29–31,43]. The SPI protein microstructures are significantly different at molecular level and in terms of physicochemical properties, i.e. polarity and water accessibility, translating in a highly different metal binding affinity.

The efficiency of these microsponges in removing the Pb^{2+} ion from aqueous solutions was evaluated by Differential Pulse Anodic Stripping Voltammetry (DP-ASV) technique. The experimental data of adsorption kinetics were processed with the pseudo first order, pseudo second order and pseudo n order kinetic equations, while Langmuir and Freundlich equations were used to process the data of isotherm adsorption. The complex adsorption mechanisms and different efficiency were explained in relation to the structural properties of the microsponges, highlighting the role of the different polarity of the internal cavities.

The presented results show the possibility of producing microsponges from Soy Protein Isolate (SPI) able to efficiently remove lead from water which can be reused in multiple cycles. The presented work highlights that general laws regulating protein self-assembly may be capitalised in the design of new eco-friendly biomaterials. Specifically, the control of properties like metal adsorption efficiency can be achieved through the modification of the final supramolecular structures. Moreover, results suggest that metal-protein-water interactions modulated by protein molecular structure may play a key role in determining the affinity of protein aggregates with metal ions.

2. Materials and methods

2.1. Reagents

Vitablend Unisol DP IP Non GMO soy protein isolate (SPI, >90 % protein) was kindly provided by Barentz ApS (Hooddorp, HB, The Netherlands). Thioflavin T ≥ 65 %, Nile Red ≥98 %, potassium phosphate monobasic ≥99 %, potassium phosphate dibasic ≥99 % were purchased from Sigma-Aldrich. Sodium nitrate and sodium chloride pure salts (Fluka) were used, after drying at 383.15 K for 2 h. Nitric and hydrochloric acids and sodium hydroxide used to adjust the pH of the Pb^{2+} ion solutions were prepared by diluting concentrated Fluka solutions. Pb^{2+} ion solutions were prepared by weighing the $Pb(NO_3)_2$ (Aldrich, analytical grade) salt. Pb^{2+} standard solutions used for calibration curves were prepared by diluting a 1000 mg L^{-1} standard solution in 2 % HNO_3 (CertiPUR, Merck). All the solutions were prepared using freshly, CO_2-free ultra-pure water (ρ ≥ 18 MΩ cm) and grade A glassware.

2.2. Samples preparation

The samples were formed by dispersing 1.5 mg mL^{-1} of soy protein in 0.1 mol L^{-1} K-phosphate buffer (final volume = 45 mL) at pH 5.0 and pH 9.0 and incubating them in 50 mL falcon tubes at 323.15 K in a water bath for 24 h. After incubation, the samples were spun down by centrifugation (7500 rpm, 10 min) and supernatant was removed. This procedure was repeated three times adding milliQ water (~25 mL) each time to remove the buffer residues. As a last step the samples were freeze dried (0.2 mbar, 233.15 K). From now on, these samples will be indicated as Soy-5 and Soy-9.

2.3. Samples characterization

2.3.1. Fourier Transform Infrared microscopy (micro-FTIR) measurements

Micro-FTIR measurements were performed at room temperature using a LUMOS Fourier Transform Infrared microscope (Bruker) equipped with a photoconductive MCT detector with liquid nitrogen cooling. Visual image collection was performed via a fast digital CCD camera, integrated in the instrument. Samples dispersed in D_2O at a final concentration of 20 mg mL^{-1}, were placed between two CaF_2 windows, separated by a 50 μm Teflon spacer. FTIR spectra were collected in the wavenumber range 4000–400 cm^{-1}. Each final spectrum was the average of 128 scans. The variable microscope aperture was set to squared regions of interest (ROIs) with a 25 μm × 25 μm size.

Fitting of the Amide I′ band was performed in terms of five Gaussian components. The Gaussian function (Eq. (1)) was used:

$$I(\nu) = \sum_{i=1}^{n} A_i \frac{1}{\sigma_i \sqrt{2\pi}} e^{\left[-\frac{(\nu-\nu_i)^2}{2\sigma_i^2}\right]} \quad (1)$$

where I is the intensity and ν_i, σ_i and A_i are the wavenumber, the width and the area of the i^{th} component, respectively. During the fitting procedure, the peak wavenumber of the selected five components was kept fixed at 1610 cm^{-1}, 1620 cm^{-1}, 1640 cm^{-1}, 1660 cm^{-1} and 1676 cm^{-1} and the spectral width was shared. The fractional area, indicating the relative amount of secondary protein structure in each spectrum, was defined by the following equation (Eq. (2)):

$$A_i\ (\%) = \frac{A_i}{\sum_{i=1}^{n} A_i} \times 100 \quad (2)$$

2.3.2. Confocal and fluorescence lifetime imaging microscopy (FLIM)

Samples with a final protein concentration of 20 mg mL^{-1} were stained with 40 μmol L^{-1} Thioflavin T (ThT) and 60 μmol L^{-1} Nile Red. 250 μL of samples were placed in microscope chambered slides and imaged at 1024 × 1024 pixel resolution, using a Leica TCS SP5 confocal laser scanning microscope and a 63× objective (Leica Microsystems, Germany). ThT was excited using λ_{ex} = 470 nm (Leica "white light laser") and the emission signal was collected in the range 485–630 nm. Nile Red was excited using λ_{ex} = 540 nm and the emission signal was collected in the range 580–700 nm. Fluorescence lifetime imaging measurements were acquired in the time domain by means of a picoHarp 300 standalone TCSPC module (Picoquant). 256 × 256 images were obtained at a scanning frequency of 400 Hz, using the aforementioned laser parameters for each dye.

2.3.3. FLIM analysis

The phasor analysis, described by Digman et al. [44] was used for FLIM data. Phasor approach is a Fourier domain technique that allows the transformation of the signal in every pixel of the image to a single point called "phasor" in the phasor plot. In this representation, all possible single exponential decays lie on the "universal circle" defined as a semicircle, with radius 1/2, going from point (0, 0), corresponding to $\tau = \infty$, to point (1, 0), corresponding to $\tau = 0$. On the contrary, complex decays are represented by phasors within the universal circle. Importantly, given that the phasors follow the vector algebra, it is possible to geometrically resolve the fractions of two fluorescent species (in the simplest case) by the lever rule of vector additions. Indeed, the linear combination of two single-exponential decay components generates phasors within the universal circle, which lie on a straight line joining the phasors of the two single components. The contribution/fraction from one single component to the lifetime is proportional to its distance from the phasor. In the phasor plot, it is also possible to select these lifetime distributions using colored cursors and the corresponding pixels will result with the same color of the cursors to the image pixels by which the so-called "lifetime maps" are obtained. FLIM data have been processed by the SimFCS software (Laboratory for Fluorescence Dynamics, University of California, Irvine, CA, available at www.lfd.uci.edu). FLIM calibration of the system for ThT was performed by measuring the known lifetime of fluorescein that is a single-exponential of 4.0 ns [45]. For Nile Red, lifetime calibration was performed using $Alexa_{594}$ that has a single-exponential lifetime of 3.9 ns [46].

2.3.4. Attenuated Total Reflectance Fourier Transform Infrared spectroscopy (ATR-FTIR)

ATR analysis on Soy-5 and Soy-9 samples, before and after Pb^{2+} adsorption, was conducted using a Bruker ALPHA FTIR spectrometer, equipped with a platinum ATR device. Spectra were recorded in the wavenumber range 4000–400 cm^{-1}, as an average of 64 scans and with a spectral resolution of 4 cm^{-1}. Background contribution was subtracted from all spectra.

2.4. Procedures for kinetic, thermodynamic and reuse experiments

The kinetic experiments of Pb^{2+} adsorption onto Soy-5 and Soy-9 samples were carried out in a voltammetric cell adding a known amount of the adsorbent material (10–20 mg) to the Pb^{2+} ions solution ($c_{Pb2+} \approx 30$ mg L^{-1}, 20 mL) at pH = 5, at I = 0.10 mol L^{-1}, in $NaNO_3$ and, only for Soy-9 sample, in NaCl, at T = 298.15 K. The suspension was constantly and regularly stirred and the metal ion concentration, always in excess in respect to Soy-5 and Soy-9 samples, was measured through differential pulse anodic stripping voltammetry (DP-ASV) measurements at various adsorbent/solution contact times in the interval 0–400 min. The voltammetric apparatus, controlled by NOVA v. 1.10 software, was constituted by a Metrohm 663 VA stand combined with the Autolab potentiostat in conjunction with the IME663 interface. The VA stand was equipped with a three-electrode system consisting of: i) a MultiMode Electrode Pro (Metrohm, code 6.1246.120) working in the Static Mercury Drop Electrode (SMDE) mode; ii) a glassy carbon auxiliary electrode (code 6.1247.000); iii) a double junction Ag/AgCl/ KCl (3 mol·L^{-1}) reference electrode (code 6.0728.030). The DP-ASV measurements were performed after bubbling purified N_2 gas into the solutions for 150 s. The experimental electrochemical conditions were chosen in order to optimize the quality parameters, as signal/noise ratio, repeatability and accuracy (deposition potential −0.55 V; deposition time 1 s; equilibration time 10 s; potential interval −0.55 to −0.20 V; scan rate 0.01 V s^{-1}; step potential 3 mV; modulation amplitude 50 mV; modulation time 0.01 s; interval time 0.2 s). The voltammetric apparatus was calibrated at the same experimental conditions of the adsorption kinetic experiments.

Isotherm experiments were carried out for Soy-5 and Soy-9 samples at initial pH = 5.00, in $NaNO_3$ 0.10 mol L^{-1} and T = 298.15 K. Only for Soy-9 sample, the isotherm adsorption experiments were extended in the pH range 4.00–6.50, at $I \rightarrow 0$ mol L^{-1} and in the ionic strength range $0.05 \leq I$ (mol L^{-1}) ≤ 0.5, in the ionic media NaCl and $NaNO_3$. All isotherm experiments were carried out in batch, at room temperature (T = 293.15 K), placing different amounts (5–20 mg) of the protein samples investigated in different Erlenmeyer flasks containing 20–40 mL of a Pb $(NO_3)_2$ solution ($c_{Pb2+} \approx 30$ mg L^{-1}) at the established experimental conditions. The suspensions were stirred at 180 rpm for 24 h using an orbital mixer (model M201-OR, MPM Instruments) and then were separated from the adsorbent material before measuring the pH and the metal ion concentration.

The reuse and recycling of Soy-5 and Soy-9 samples were studied by packing ~5 mg of the adsorbent into a glass column (diameter = 2 cm, length = 10 cm). A volume of 15 mL of $Pb(NO_3)_2$ solution ($c_{Pb2+} \approx 30$ mg L^{-1}, pH = 5, T = 298.15 K) was flowed at reflux into the column with a flow rate of 6 mL min^{-1} for 16 h (the reaching of adsorption equilibrium was verified) by using a peristaltic pump (Gilson, Minipuls 3). The sorbent material was then washed with 100 mL of distilled water before the reflux with 15 mL of EDTA 0.1 mol L^{-1} solution for 7 h. After a further washing with 100 mL of distilled water, the next adsorption/desorption cycle began. The solutions derived from each adsorption/desorption step were collected in test tubes. Four adsorption/desorption cycles were carried out. The metal ion concentrations in the solutions collected in isotherm and in the adsorption steps of reuse experiments were measured by the same voltammetric apparatus previously used in kinetic experiments. Due to the presence of EDTA, some experimental electrochemical conditions of the voltammetric cell were modified to measure the lead concentrations in solutions derived from desorption steps (deposition potential −1.15 V; deposition time 90 s; potential interval −1.15 to −0.20 V). The voltammetric cell was previously calibrated at the same experimental conditions of the analyzed solutions.

The pH of the solutions collected during the adsorption experiments was measured with a combined ISE-H^+ glass electrode (Ross type 8102) previously calibrated at the same experimental conditions.

2.5. Kinetic and isotherm models for Pb^{2+} adsorption onto Soy-5 and Soy-9 samples

The kinetic data of Pb^{2+} ions adsorption onto the Soy-5 and Soy-9 samples were tentatively fitted with three kinetic models: i) the most used pseudo-first order (PFO) [47] (Eq. (3)) and ii) pseudo-second order (PSO) [48] (Eq. (4)) equations and iii) the pseudo n order equation (PGO) [49] (Eq. (5)). The relevant integrating non-linear equations for the boundary conditions $t = 0$ to $t = t$ and $q_t = 0$ and $q_t = q_t$ used in data processing are listed below (Eqs. (3)–(5)):

$$q_t = q_e \left(1 - e^{-k_1 t}\right) \quad (3)$$

$$q_t = \frac{q_e^2\, k_2\, t}{1 + q_e\, k_2 t} \tag{4}$$

$$q_t = q_e - \frac{q_e}{\left(k_n q_e^{(n-1)} t(n-1) + 1\right)^{\frac{1}{(n-1)}}} \text{ with } n \neq 1 \tag{5}$$

where q_t and q_e are the adsorption capacity of the adsorbent material (mg g^{-1}) at adsorbent/solution contact time t and at the equilibrium, k_1 (min^{-1}), k_2 (g mg^{-1} min^{-1}) and k_n (min^{-1} (g mg^{-1})$^{n-1}$) are the rate constants of the PFO, PSO and PGO models, respectively and n represents the general order of adsorption of the PGO model.

The adsorption equilibria data at different experimental conditions have been processed with the Freundlich [50] (Eq. (6)) and Langmuir [51] (Eq. (7)) isotherm models:

$$q_e = K_F\, c_e^{1/n} \tag{6}$$

$$q_e = \frac{q_m\, K_L\, c_e}{1 + K_L\, c_e} \tag{7}$$

where q_m (mg g^{-1}) is the maximum adsorption capacity of the Soy-5 and Soy-9 samples, c_e (mg L^{-1}) is the Pb^{2+} ions concentration in solution at equilibrium; K_F ($L^{1/n}$ g^{-1} $mg^{1-1/n}$) and K_L (L mg^{-1}) are the Freundlich and Langmuir constants, respectively.

The Pb^{2+} ions adsorption capacity at different contact times (q_t) in kinetic studies or at adsorption equilibrium q_e at different Pb^{2+}/protein aggregate ratios in the isotherm experiments were calculated by the following equation (Eq. (8)):

$$q_t or\ q_e = \frac{V\,(c_0 - c_t)}{m} \tag{8}$$

where V (L) is the volume of the Pb^{2+} ion solution and m is the mass of Soy-5 and Soy-9 samples (g); c_0 and c_t are the Pb^{2+} ion concentrations in the solutions (mg L^{-1}) at $t = 0$ and $t = t$, respectively. At equilibrium, Eq. (8) was used by replacing c_t with c_e to calculate q_e.

The LIANA and OriginLab suite software (OriginLab Corporation, Northampton, Massachusetts, USA) were used to fit kinetic and isotherm equations to experimental data.

3. Results and discussion

3.1. Characterization of secondary protein structure by Fourier Transform Infrared microscopy (micro-FTIR)

Soy protein isolate was treated at high temperature in order to obtain protein microstructures with different structural properties. The two different samples were produced by incubating 1.5 mg mL^{-1} of protein solution in phosphate buffer (0.1 mol L^{-1}) pH 5.0 and pH 9.0 at 323.15 K for 24 h. After washing procedures, the samples were freeze dried (see methods for details) to obtain stable powders.

In Fig. 1 a) and b) we report the 360 μm × 280 μm optical images of the Soy-5 and Soy-9 samples, respectively, dispersed in D_2O solution at a concentration of 20 mg mL^{-1}. Micron-sized protein aggregates are present in both samples. Interestingly, the Soy-5 sample has a darker appearance with respect to the Soy-9 sample, which is translucent. This suggests that the microparticles are characterized by different refractive index and that the darker color could be attributed to a more compact structure in the Soy-5 sample [52]. The different optical properties reflected by opacity or transparency of the aggregates can be related to differences in water retention capacity and to different structural features or levels of order [52].

To verify that, we acquired micro-FTIR absorption spectra at single aggregate level in the 25 μm × 25 μm ROIs, indicated by the colored squares in panel a) and b) of Fig. 1. Spectra in the Amide I′ region (1710 cm^{-1}–1570 cm^{-1}) for Soy-5 sample (pink line) and Soy-9 sample (green line) are shown in Fig. 1 c). Data are normalized to the band area and the selected Gaussian components used for the deconvolution of these spectra are also shown.

The Amide I′ spectral region contains information about protein secondary structure. The detailed analysis of this peak can provide

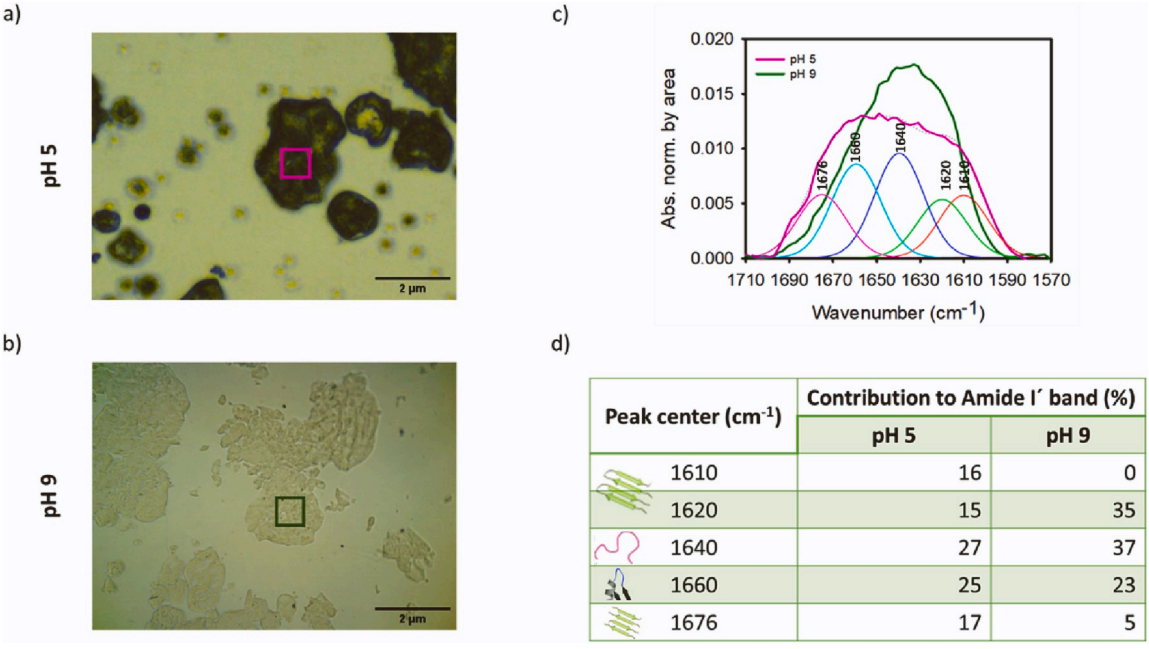

Peak center (cm^{-1})	Contribution to Amide I′ band (%)	
	pH 5	pH 9
1610	16	0
1620	15	35
1640	27	37
1660	25	23
1676	17	5

Fig. 1. Representative 360 μm × 280 μm optical images for soy samples (a) Soy-5 and (b) Soy-9 sample, in D_2O. The colored 25 μm × 25 μm squares represent the ROIs where FTIR spectra were collected. (c) FTIR spectra in the Amide I′ region (1710–1570 cm^{-1}) acquired in each ROI of each image, following the same color code. No significant differences, in terms of spectral shape, were observed by varying ROI position or size within the different microscopic aggregates or within the same aggregate. Representative spectral deconvolution of FTIR spectrum for Soy-5 sample in five Gaussian components with spectral components centred at 1610 cm^{-1}, 1620 cm^{-1}, 1640 cm^{-1}, 1660 cm^{-1} and 1676 cm^{-1}. Each component is assigned to a specific protein secondary structure. (d) Fractions of the total area of the Amide I′ spectral region for each of the components used for the deconvolution.

information on the orientation of β-strands forming the intermolecular β-sheets (parallel vs antiparallel), and the strength of inter-strand hydrogen bonds or the number of strands composing the sheet [53]. Soy-9 sample presents a narrower peak, centred at around 1640 cm^{-1}, while the spectrum of Soy-5 sample appears to be significantly broader indicating a larger structural heterogeneity. The Amide *I'* deconvolution for the two samples was performed using five Gaussian components, namely 1610 cm^{-1}, 1620 cm^{-1}, 1640 cm^{-1}, 1660 cm^{-1}, 1676 cm^{-1} (Fig. 1c) and results of the fit are reported in Fig. 1 d). This fit is aimed at comparing the two aggregate species, highlighting the presence of native and aggregated structures. The 1610 cm^{-1} and 1620 cm^{-1} peaks are assigned to intermolecular β-sheets [53,54], which often represent the fingerprint of amyloid-like structures. The component at 1610 cm^{-1} is aimed at representing the presence of intermolecular β-structure components with stronger H-bonds or longer β-chains [55,56]. 1640 cm^{-1} component is assigned to random coils and 1660 cm^{-1} to turn and loops. The peak at 1676 cm^{-1} is assigned to antiparallel intermolecular β-sheets.

Both samples present a similar and high content of random coils (peak at 1640 cm^{-1}), turns and loops (peak at 1660 cm^{-1}) in line with what was previously reported for native SPI [57]. From the presented analysis it is possible to note that the total content of intermolecular β-structures is similar between the two samples (48 % for Soy-5 sample and 40 % for Soy-9 sample). However, the peak at 1620 cm^{-1}, which can be attributed to intermolecular parallel β-sheets typical of amyloids, is dominant for Soy-9 sample, while the representative component used to describe stronger H-bonds (1610 cm^{-1}) is not present. Soy-5 sample presents all the components assigned to intermolecular β-sheets; 1610 cm^{-1} (16 %), 1620 cm^{-1} (15 %) and 1676 cm^{-1} (17 %), with similar contribution.

The structural differences between the samples may affect metal affinity, as amyloid β-structures were identified as key aspects to remove toxic heavy metal ions from water [25,26,33,35,58].

3.2. Quantitative fluorescence microscopy for probing morphological and structural features

In order to gain more information on characteristic features of the samples at high spatial resolution, confocal fluorescence microscopy and fluorescence lifetime imaging measurements were performed on ThT stained samples and results are reported in Fig. 2. ThT is the gold standard fluorescence dye used to specifically characterize amyloid structures and its fluorescence lifetime was shown to be sensitive to the details of the intermolecular β-sheets arrangement [59–61].

In Fig. 2 a) representative 1024 × 1024 confocal fluorescence microscopy images of Soy- 5 and Soy-9 samples in water, stained with ThT are shown. Both samples present heterogeneous, micron-sized sponge-like structures with different shapes and sizes. The ThT fluorescence intensity signal for each sample reveals the absence of significant differences in the structural organization within submicron scale. However, in the same experimental conditions, a difference in ThT fluorescence intensity is observed between the two samples with the ThT fluorescence intensity of Soy-9 sample being significantly lower. We retrieved the ThT fluorescence intensity in different ROIs in the images of the two samples and the values are reported in the histograms in Fig. 2 b). This difference can be ascribed to different affinity or accessibility of the dye within the aggregates, differences in the rigidity in ThT environment and/or to distinct molecular features of "below resolution" amyloid structures as sensed by this dye.

In Fig. 2 c) we report results of FLIM measurements analyzed by means of the phasor approach. It is a simple Fourier Transform domain technique, which allows, without fitting procedures, the transformation of the signal in every pixel of the image, to a point in a polar plot corresponding to the measured fluorescence lifetime. All the possible single exponential lifetimes lie on the universal circle, while complex decays are represented by phasors within the circumference. Fig. 2 c) demonstrates the presence of two distinguishable ThT lifetime distributions for the two samples located within the universal circle (the qualitative

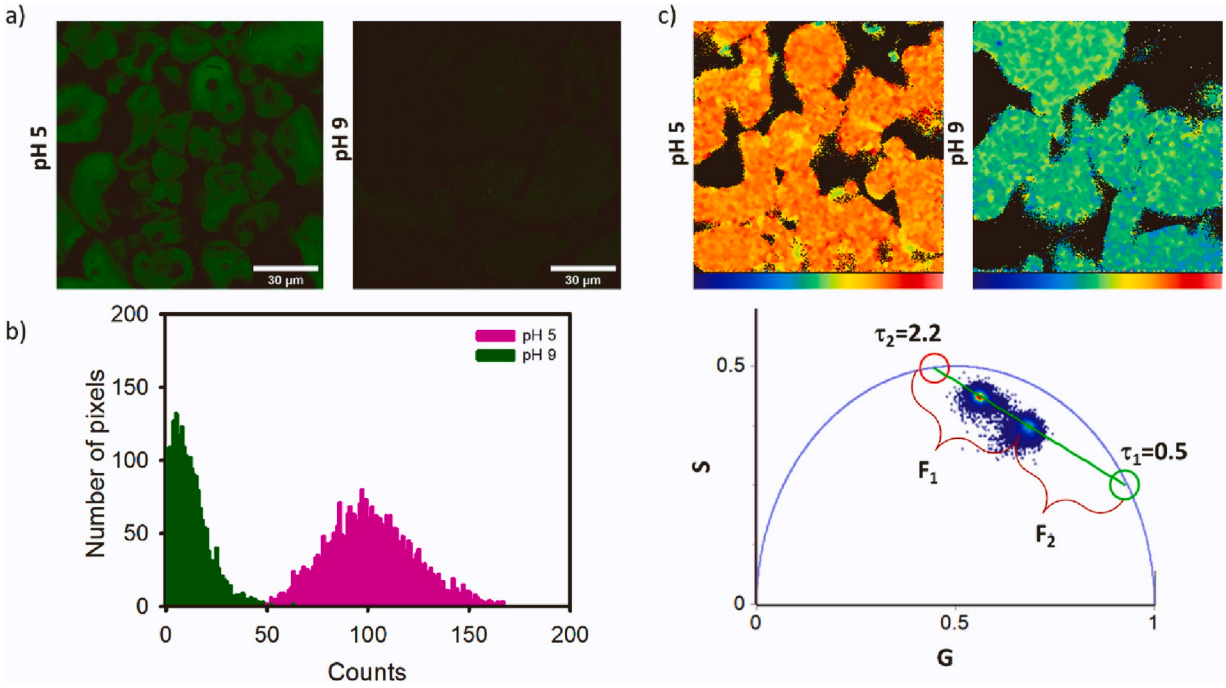

Fig. 2. (a) 1024 × 1024 representative confocal fluorescence microscopy images of Soy-5 and Soy-9 samples in water, stained with 40 μM ThT at the same experimental conditions. (b) Histogram of the average intensity of ThT fluorescence intensity in the two images. (c) Phasor analysis of FLIM measurements on Soy-5 and Soy-9 samples stained with ThT in water solution. The signal is acquired under laser excitation at 470 nm, in the range 485–630 nm. Data analysis is performed using a double exponential decay whose principal components are $\tau_1 = 0.5$ ns (green) and $\tau_2 = 2.2$ ns (red) identified drawing a straight line interpolating the two lifetime distributions evident in the phasor plot. Lifetime fraction map for the FLIM image colored according to F_1 (fractional contribution of the faster component). Image size is 256 × 256.

analysis of the data is reported in Supporting Materials, Fig. SM1). In the phasor representation, a double exponential decay lies on the line connecting two characteristic single exponential phasors on the universal circle. The distance between each point of the cloud and the single exponential phasor represents the fraction of each component. As previously reported [62], it is possible to analyze ThT fluorescence decays using a double exponential decay. The fastest component can be attributed to less specific interaction between ThT and its environment due to increased environmental viscosity, while the slower decay is attributed to more specific interaction between ThT and intermolecular β-structures [62,63]. As shown in Fig. 2 c), this is possible also for the analysis of the present samples: a straight line passes through the characteristic lifetime distributions of the two samples and connects two single exponential lifetimes identified as $\tau_1 = 0.5$ ns (green circle) and $\tau_2 = 2.2$ ns (red circle). These lifetime values are compatible with the ones previously described for ThT lifetime decay [62,63].

Using this model, the decay will be described as:

$$I(t) = F_1 e^{-\frac{t}{\tau_1}} + F_2 e^{-\frac{t}{\tau_2}} \quad (9)$$

where F_1 and F_2 are the fraction of the single exponential decays with τ_1 and τ_2 representing the fast and slow average lifetimes. FLIM images are colored in false colors according to the F_i fraction of the τ_i component. The scale goes from blue (pure fast component at $\tau_1 = 0.5$ ns) to red (pure slow component at $\tau_2 = 2.2$ ns). As expected, aggregates in the image present uniform lifetime within the same sample and the fastest decay is dominant in Soy-9 sample ($F_1 = 0.50$), when compared with Soy-5 sample ($F_1 = 0.29$), indicating a more tightly packed organization of β-structures in the Soy-5 sample, which is in line with the FTIR measurements.

With the idea of using these aggregates as sponge-like structures to purify water from Pb^{2+} ions, we investigated their water accessibility and hydrophobicity, by means of the fluorescent dye Nile Red. Nile Red is an uncharged hydrophobic dye and its fluorescence properties depend on the polarity of the environment in its surroundings. It is known to interact with hydrophobic cavities in native proteins and it is widely used to detect and characterize the exposure or formation of new hydrophobic surfaces during formation of aggregates [64]. Specifically, the fluorescence lifetime of this dye is reduced in more polar environments [65]. In Fig. 3, the phasor analysis of FLIM measurements is reported for Nile Red stained samples dispersed in water.

In Fig. 3 a) the phasor plot is shown, where the presence of two lifetime distributions is highlighted by colored circles. Fig. 3 b) and c) report the representative 256 × 256 pixel intensity images acquired for b) Soy-5 sample and c) Soy-9 sample, while in Fig. 3 d) and e) the corresponding lifetime maps are reported. In these images, pixels are colored according to their lifetime in the phasor plot; as a one-to-one correlation exists between the pixels in the image and their phasors, it is possible to select pixels in the phasor plot using a colored circle and they will appear in the same color in the image. Soy-5 and Soy-9 samples are characterized by two distinguishable fluorescence lifetime distributions in the phasor plot.

In the present conditions, single exponential decays are observed. Nile Red fluorescence decay with the shorter lifetime (pink cursor: $\tau_i = 3.9$ ns) characterizes the Soy-5 sample while in Soy-9 sample the fluorescence decay of the dye is characterized by a longer lifetime (green cursor $\tau_i = 4.9$ ns). Uniform lifetime distribution for Nile red is observed within the same sample despite of inhomogeneity in fluorescence intensity. The shorter lifetime observed in Soy-5 indicates that the hydrophobic binding sites are characterized by higher polarity.

Controversial explanations exist regarding the role of water molecules in metal binding. Some works demonstrated that water molecules might participate in metal binding by stabilizing metals in a particular conformation [66]. Others, proposed that protein-metal interactions are stronger in media with reduced dielectric constant [67]. In accordance with the latter theory, our result suggests that Soy-9 may present an increased metal binding efficiency.

3.3. *Soy microsponges - Pb^{2+} ion interactions studied by Attenuated Total Reflectance-Fourier Transform Infrared (ATR-FTIR) spectroscopy*

To investigate whether specific interactions exist between Pb^{2+} ions and the soy micronsponges, we performed ATR-FTIR measurements on freeze dried Soy-5 and Soy-9 samples before and after the interaction with Pb^{2+} ions. Samples (10–20 mg) were incubated at room

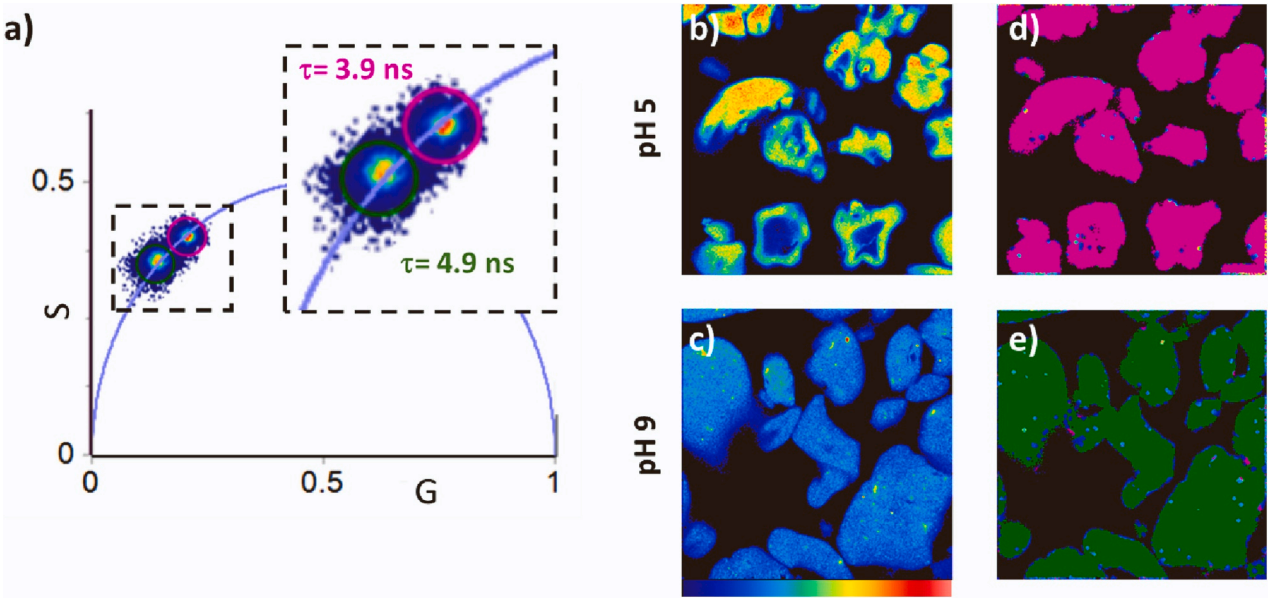

Fig. 3. (a–e) Phasor analysis of FLIM measurements on Soy-5 and Soy-9 samples stained using Nile red (60 μM). The signal was acquired under laser excitation at 540 nm and collected in the range 580–700 nm. (a). Phasor plot showing two different lifetime distributions, highlighted by colored circular cursors. A magnification of the region highlighting the area of interest is reported in the dashed lines surrounded inset. (b–c) Intensity map of Nile Red in (b) Soy-5 sample and (c) Soy-9 sample. (d–e) Lifetime maps corresponding to (b) and (c) measurements respectively, in which the pixels are colored accordingly to the color cursors used in the phasor plot.

temperature and in identical conditions at room temperature in 20 mL of 30 mg L^{-1} Pb^{2+} metal ions solution for 12 h, then separated from the solution and freeze dried.

In dried state it is possible to investigate specific spectral regions of interest for protein-metal binding sites. Fig. 4 a) and b) reports the ATR-FTIR spectra of Soy-5 and Soy-9 samples before and after the incubation with Pb^{2+} solution. Protein aggregates may contain both specific and not specific metal binding sites including negatively charged (Asp, Glu) or polar (Cys, His and Asn) residues. Specifically, it is expected that an attraction between the electron-rich atoms such as O, N and S and electron-deficient metal ions exists. Thus, thiolate (—S—), carboxylate (—COO—), and amine (—NH—) groups may be involved in metal binding. By comparing the spectra of both samples before and after exposure to aqueous solution containing Pb^{2+} ions, variations are observed in the low wavenumber spectral region. Both Soy-5 and Soy-9 samples containing Pb^{2+} ions present the growth of two new peaks at the region around 1350 cm^{-1} (pink region) and 835 cm^{-1} (green region). The peak at about 1350 cm^{-1} is assigned to the specific interaction, generated by the binding between Pb^{2+} ions and the O—H of the carboxylic acid and C—N of the amino group [68]. The peak at 835 cm^{-1} can be attributed to interaction of Pb^{2+} ions with S atoms in the polypeptide chain [69]. The interaction of Pb^{2+} ions with the S atoms of Soy-5 sample is also demonstrated by a pronounced peak at 976 cm^{-1} [25,70].

3.4. Kinetics of Pb^{2+} ions adsorption onto Soy microsponges

The kinetics of Pb^{2+} ions adsorption onto Soy-5 and Soy-9 samples have been studied in $NaNO_3$ at $I = 0.1$ mol L^{-1}, at pH = 5 and at $T = 298.15$ K. Only for Soy-9 sample the studies have been extended to NaCl medium at the same experimental conditions. Three kinetic models, namely PFO, PSO and PGO (see Methods section), have been used to fit the experimental data (see Fig. 5 and Fig. SM2 of Supporting material).

The parameters values of the three kinetic models together with the statistical parameters R^2 and std. dev. values of fits are reported in Table 1, while the kinetic parameters values of the best model in terms of goodness of fit are reported in the histograms of Fig. 6.

All the adsorbent materials investigated reached the adsorption equilibrium quickly. In particular, Soy-9 sample needs almost 50 min, while Soy-5 sample reaches the adsorption equilibrium within ~25 min.

Looking at the first two kinetic models considered, the PSO equation fits the experimental data of the two adsorbent materials better than the PFO (highest R^2 and lowest σ values), suggesting, at least, a second order kinetics of Pb^{2+} adsorption. Extending the analysis to the third kinetic model, the statistical parameters values of the fits show that also the PGO model fits quite well with the experimental data. For this reason, additional comments based on the kinetic parameters derived from the PGO equation can be made.

The PGO model has been already used by several authors [71–73]. Unlike the other two models, the PGO equation provides a non-predetermined reaction order (n). The reaction order is closely related to the characteristics of the adsorbent (structure, conformation, number and type of available binding sites) as well as to the experimental conditions of the adsorbent – metal ion system, such as ionic medium, ionic strength, and pH that influence all the aforementioned adsorbent characteristics. The intrinsic properties of protein microsponges suggest an increase of adsorption sites available to bind the metal ion. These sites include specific amino acidic sidechains, the already present binding sites in the native soy protein isolate, typical of amyloid structures, and new hydrophobic cavities that could be responsible of a kinetic order of adsorption higher than two [72,73]. The refined n value obtained for Soy-9 in $NaNO_3$ medium is 2.04. This value is higher if compared with the pseudo-first order previously found for Soy protein hollow microspheres [14], confirming that the structural characteristic of the adsorbent and the experimental conditions are crucial [10].

Moreover, considering the experimental errors, comparable values of kinetic constants have been calculated by PSO and PGO models in this ionic medium (see Table 1). This means that for the Pb^{2+} ions adsorption onto Soy-9 protein microsponges the PGO and PSO models are equivalent, confirming a pseudo second order kinetic of adsorption. The comparable n and k_n values calculated for Soy-9 sample in $NaNO_3$ and NaCl media indicate that the kinetic of adsorption is not influenced by the ionic composition of the metal ion solution. On the contrary, the ionic medium composition affects the adsorption ability of the adsorbent at equilibrium, which decreases in NaCl ($q_e = 38.49$ and 28.59 mg g^{-1} in $NaNO_3$ and NaCl, respectively). This is probably due to the formation of lead-chloride species that changes the chemical speciation profile of the metal ion reducing the percent of Pb^{2+} ions in solution.

The statistical testing parameters (R^2 and std. dev. of fit) values indicate the PGO model as that with the best fit for Soy-5 sample. Moreover, the kinetic constant (k_n) and the reaction order n calculated do not agree with those refined (k_2) or fixed (2) in the PSO model. In particular, different constant ($k_n = 0.005$ min^{-1} (g $mg^{-1})^{n-1}$) and reaction order ($n = 2.72$) have been calculated. This indicates that the kinetics of metal ion uptake by Soy-5 sample are more complex as they have a fractional reaction order higher than 2.

The adsorption kinetics of Soy-5 is comparable with that previously reported for the adsorption of the same metal ion onto amyloid particulates of BSA at the same pH, toxic metal ion concentration and ionic strength [25] this confirming that generic features of protein molecule

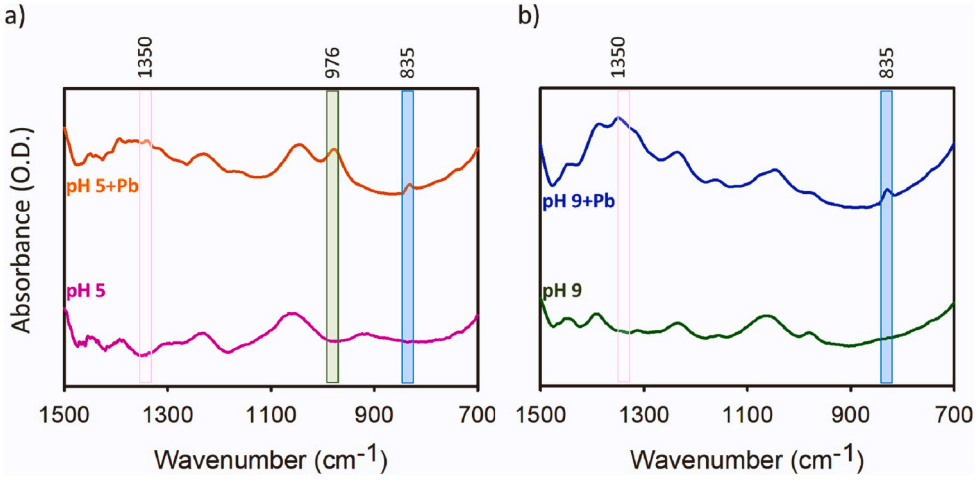

Fig. 4. ATR-FTIR spectra, acquired in the range 1500–700 cm^{-1}, of freeze-dried a) Soy-5 and b) Soy-9 samples before and after the interaction with Pb^{2+}. Color bands are used to highlight the spectral regions where significant variations are observed.

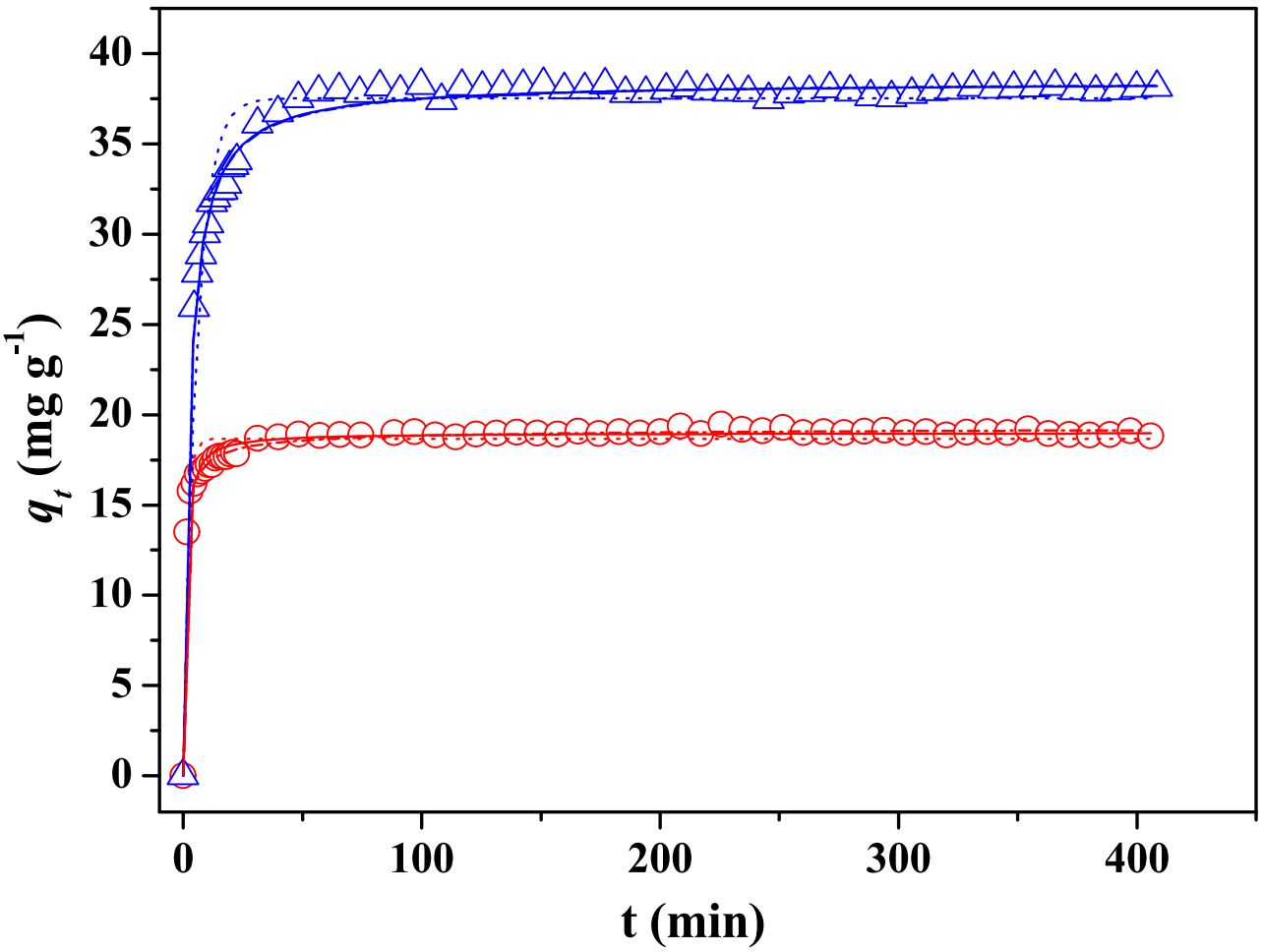

Fig. 5. Dependence of q_t (mg g^{-1}) on contact time for the Pb^{2+} adsorption onto 19.2 mg of Soy-5 sample (■) and 11.2 mg of Soy-9 sample (△). Data are fitted with PFO (dotted line) PSO (continuous line), and PGO (dashed/dotted line) kinetic models. Other experimental conditions: 20 mL of aqueous solution containing $NaNO_3$ 0.10 mol L^{-1}; $Pb(NO_3)_2$ (c_{Pb2+} = 30 mg L^{-1}), pH = 5.0, T = 298.15 K.

may regulate Pb^{2+} uptake. Specifically, BSA particulates, like Soy-5, adsorbed Pb^{2+} ions following kinetics of pseudo general order model with a refined reaction order value between 2.75 and 3.14. The lower kinetic order of Pb^{2+} ions adsorption onto Soy-9 ($2.084 \leq n \leq 2.14$) is presumably attributable to the less packed organization of β-structures in the Soy-9 sample (see Section 3.2).

Under the experimental conditions of the kinetic experiments, the equilibrium adsorption capacities (q_e) of the microsponges in $NaNO_3$ 0.1 mol L^{-1} have the following trend: Soy-9 sample > Soy-5 sample (see Fig. 6). This indicates that the observed differences in the structures of SPI microsponges, obtained only by incubating the protein isolate at two different pH in aqueous solution, play an important role on the performance of the adsorbent material. In particular, the q_e of protein sample increases for SPI microsponges produced at pH 9. However, this is only a rough estimate considering the different amounts of Soy-5 and Soy-9 samples used in the kinetic experiments (~19 mg of Soy-5 sample and ~11 mg of Soy-9 sample). This aspect will be discussed in detail in the next section.

3.5. Adsorption equilibria of Pb^{2+} ions onto Soy microsponges

The thermodynamics of Pb^{2+} ion adsorption onto SPI microsponges have been studied through a series of batch adsorption experiments at different experimental conditions, namely pH range 4.0–6.5, without ionic medium or with the addition of $NaNO_3$ or NaCl, at different ionic strengths ($0.10 \leq I/\text{mol L}^{-1} \leq 0.50$), and at T = 298.15 K. The experimental data were then processed with the Langmuir and Freundlich isotherm models. The parameters of the models were subsequently analyzed in order to obtain information regarding the maximum adsorption capacities and affinities of Soy microsponges towards the toxic metal ion. The fitting curves of the experimental data (q_e vs c_e) using Langmuir and Freundlich isotherm equations are depicted in Fig. 7 and in Figs. SM3–SM5 of Supplementary material.

The values of the parameters of the two isotherm equations are reported in Tables 2 and 3 together with the statistical parameters of fits R^2 and σ and in the histograms of Figs. 8 and 9 for an easier comparison. Both models fitted quite well the experimental data, though in most cases the fits with Langmuir model showed a slightly higher R^2 and lower σ.

A first set of batch experiments was carried out to study the adsorption equilibria of Pb^{2+}/Soy-5, and Pb^{2+}/Soy-9 systems at the same experimental conditions ($c_{Pb2+} \approx$ 30 mg L^{-1}, pH = 5, $NaNO_3$ medium, I = 0.1 mol L^{-1} and T = 298.15 K) with the aim to establish which of the prepared protein microsponges was the best adsorbent of Pb^{2+} ions.

The results of adsorption isotherms substantially confirm the q_e trend obtained through kinetic experiments at a single adsorbent/metal ion ratio. Specifically, both the maximum adsorption capacity (q_m) and affinity (K_L) are larger for Soy-9 sample with respect to Soy-5, reaching the q_m value of 37.74 mg g^{-1} and a K_L equal to 0.97 L mg^{-1} for Soy-9 sample (see Fig. 8).

The balance between specific binding sites, which are diversified in

Table 1
Parameters of PFO, PSO and PGO kinetic equations for Pb^{2+} adsorption on Soy-5 and Soy-9 samples, at pH = 5.0, in $NaNO_3$ 0.1 mol L^{-1} and at T = 298.15 K.

Sorbent	PFO parameters		R^2	σ[a]
	q_e[b]	k_1[c]		
Soy-5	18.656 ± 0.095[d]	0.686 ± 0.056[d]	0.9256	0.7111
Soy-9	37.52 ± 0.20	0.180 ± 0.008	0.9396	1.3782
Soy-9[e]	27.55 ± 0.18	0.110 ± 0.006	0.9383	1.2005

Sorbent	PSO parameters		R^2	σ[a]
	q_e[b]	k_2[f]		
Soy-5	18.998 ± 0.044	0.0703 ± 0.0034	0.9874	0.2927
Soy-9	38.429 ± 0.081	0.0105 ± 0.0003	0.9923	0.4908
Soy-9[e]	28.38 ± 0.12	0.0077 ± 0.0004	0.9810	0.6663

Sorbent	PGO parameters			R^2	σ[a]
	q_e[b]	k_n[g]	n		
Soy-5	19.38 ± 0.07	0.017 ± 0.004	2.72 ± 0.11	0.9949	0.1856
Soy-9	38.49 ± 0.15	0.009 ± 0.002	2.040 ± 0.089	0.9922	0.4943
Soy-9[e]	28.59 ± 0.28	0.005 ± 0.002	2.14 ± 0.15	0.9808	0.6691

[a] std. dev of the fit.
[b] mg g^{-1}.
[c] min^{-1}.
[d] ±std. dev.
[e] In NaCl 0.1 mol L^{-1}.
[f] g mg^{-1} min^{-1}.
[g] min^{-1} (g mg^{-1})$^{n-1}$.

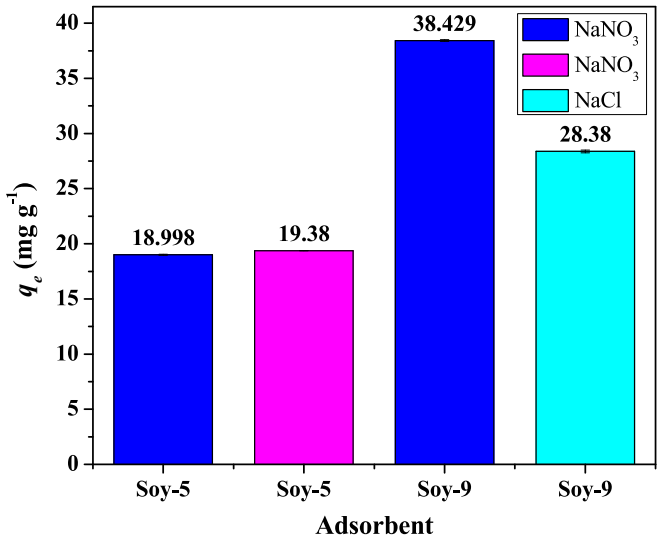

Fig. 6. q_e values of PSO (blue or cyan bars) and PGO (magenta bars) kinetic equation for the Pb^{2+} adsorption onto Soy-5 and Soy-9 samples from aqueous solutions containing different ionic media, at I = 0.1 mol L^{-1}, at pH = 5.0 and at T = 298.15 K.

the two samples (see Fig. 4), different water accessibility, and polarity of the internal cavities contribute to the observed different behavior.

Structural and physicochemical properties of the samples have to be taken into account to explain this difference. Indeed, as shown in previous sections, the two adsorbents not only differ in the molecular structure, but also in the polarity of accessible cavities, with Soy-5 sample being characterized by a higher polarity. Soy-9 sample presents the typical amyloid peak centred at 1620 cm^{-1} in FTIR spectrum, indicating the presence of a significant amount of parallel intermolecular β structures (35 %), while antiparallel β structures are present in

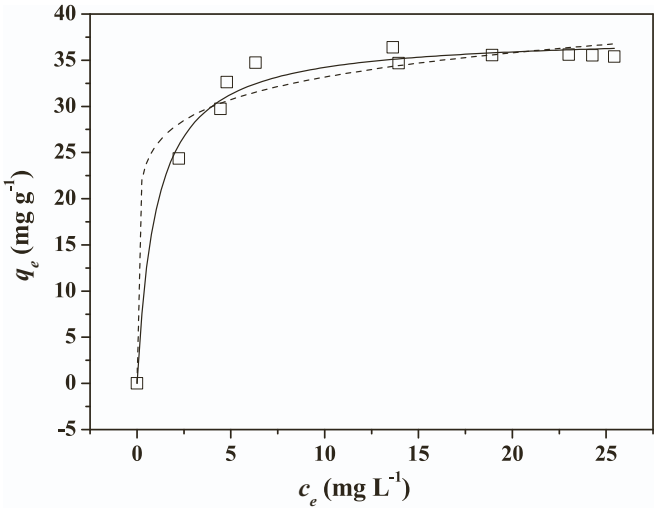

Fig. 7. Adsorption isotherm of Pb^{2+} ions onto Soy-9 sample from aqueous solutions containing $NaNO_3$ 0.10 mol L^{-1}, at pH = 5.00 and T = 298.15 K. Experimental data fitted with Freundlich (dashed lines) and Langmuir (continuous lines) isotherm equations.

lower amount. Soy-5 sample presents a more heterogeneous structure where strong intermolecular β-sheets (16 %) are also present, possibly with reduced intermolecular distances between strands. This may change water accessibility and, consequently, metal accessibility to the internal parts of the aggregates. In addition, the whole Soy-5 microsponges structures are characterized by a higher polarity in water and this may affect the affinity. In line with that, we have previously suggested that protein and metal hydration water may play a significant role in Pb^{2+} ions adsorption from protein aggregates [25]; local interactions between water molecules and the polar and nonpolar regions in protein may modify protein hydration thus regulating occurring interactions [66]. Indeed, water molecules may also participate in metal binding and stabilize the metals in a particular conformation [59].

At this point, investigation on Soy-9 has been extended to other experimental conditions changing the pH, the ionic medium and the ionic strength of the Pb^{2+} aqueous solutions.

Experimental conditions of the toxic metal ion solution can critically affect the adsorption performances of the adsorbent material used in decontamination treatments for several reasons: i) low pH values can cause partial or total protonation of binding groups of the protein microsponges (—COOH, —NH_2, —SH) as well as high pH values lead to the formation of hydrolytic species of Pb^{2+} ions ($Pb(OH)^+$, $Pb(OH)_2$, $Pb(OH)_3^-$ and other polynuclear hydrolytic species not present at the Pb^{2+} concentrations used in this work); ii) the ions coming from the ionic medium dissociation could form ion pairs or weak complexes with some of the binding groups of the adsorbent as well as with the Pb^{2+} ions ($PbCl^+$, $PbCl_2$, $PbCl_3^-$, PbCl(OH)); moreover they can produce adsorbent modifications; iii) the increase of ionic strength, mainly related to the ionic medium concentration, enhances the background salt effects listed in previous point [74–76].

The adsorption isotherm of Pb^{2+} ions onto Soy-9 sample at pH = 4 showed an unusual trend (see Fig. SM4 a)). In fact, at a fixed metal ion concentration ($c_{Pb2+} \approx$ 30 mg L^{-1}), the adsorption capacity of the protein microsponges, at first, increases as the amount of Soy-9 sample decreases, reaching a maximum and then rapidly going to zero. This anomalous trend can be attributed to structural modifications and destabilisation of the protein microsponges. Indeed, a subtle interplay between long range electrostatic forces, hydrophobic interactions and short-range protein - protein interactions is involved in the stability of protein aggregates. The pH value of 4 is critically different from the pH in which the Soy-9 aggregates are formed and, in particular, is on the opposite side with respect to the isoelectric point. As previously reported

Table 2
Freundlich and Langmuir isotherm parameters for the Pb^{2+} ions adsorption onto Soy-5 and Soy-9 samples from Pb^{2+} (c^{2+}_{Pb} = 30 mg L^{-1}) aqueous solutions at pH = 5.0, in $NaNO_3$ 0.10 mol L^{-1} and at T = 298.15 K.

Adsorbent	pH_i[a]	pH_f[a]	Langmuir paramaters				Freundlich parameters			
			q_m[b]	K_L[c]	R^2	σ[d]	K_F[e]	n	R^2	σ[d]
Soy-5	5.02	4.93	23.16 ± 0.61[f]	0.386 ± 0.033[f]	0.9945	1.3712	8.75 ± 0.25[f]	3.02 ± 0.14[f]	0.9961	0.9714
Soy-9	5.00	5.61	37.74 ± 0.72	0.97 ± 0.15	0.9863	14.1018	25.7 ± 1.7	9.1 ± 2.0	0.9643	36.760

[a] Mean values of initial and final pH of Pb^{2+} solutions used in isotherm experiments.
[b] In mg g^{-1}.
[c] In L mg^{-1}.
[d] std. dev of the fit.
[e] $L^{1/n}$ g^{-1} $mg^{1-1/n}$.
[f] ±std. dev.

Table 3
Freundlich and Langmuir isotherm parameters for the Pb^{2+} adsorption onto Soy-9 sample from Pb^{2+} (c^{2+}_{Pb} = 30 mg L^{-1}) aqueous solutions containing different ionic media, at different ionic strengths and pH and at T = 298.15 K.

Medium	I/mol L^{-1}	pH_i[a]	pH_f[a]	Langmuir parameters				Freundlich parameters			
				q_m[b]	K_L[c]	R^2	σ[d]	K_F[e]	n	R^2	σ[d]
–	→ 0	4.95	5.50	36.40 ± 0.53[f]	0.768 ± 0.093[f]	0.9858	1.2444	21.3 ± 1.9[f]	6.9 ± 1.3[f]	0.9293	2.7761
$NaNO_3$	0.10	5.00	5.61	37.74 ± 0.72	0.97 ± 0.15	0.9863	14.1018	25.7 ± 1.7	9.1 ± 2.0	0.9643	36.760
$NaNO_3$	0.10	6.54	5.92	56.2 ± 2.1	0.211 ± 0.036	0.9726	2.2903	23.9 ± 2.3	4.88 ± 0.74	0.9653	2.5757
$NaNO_3$	0.50	4.95	5.53	22.6 ± 3.2	0.40 ± 0.16	0.9676	1.0512	8.05 ± 1.30	2.57 ± 0.69	0.9605	1.1597
NaCl	0.05	4.99	5.69	33.18 ± 0.61	0.92 ± 0.13	0.9919	0.8680	21.7 ± 1.3	7.6 ± 1.4	0.9806	1.3401
NaCl	0.10	4.99	5.72	29.8 ± 1.3	0.62 ± 0.17	0.9763	1.4267	18.1 ± 1.5	7.1 ± 1.6	0.9750	1.4660
NaCl	0.30	4.98	5.92	16.57 ± 0.53	0.677 ± 0.076	0.9920	0.3981	6.75 ± 0.35	2.51 ± 0.22	0.9808	0.6188
NaCl	0.50	4.97	6.04	11.6 ± 1.7	0.46 ± 0.14	0.9582	0.4972	3.65 ± 0.32	1.84 ± 0.30	0.9345	0.6223

[a] Mean values of initial and final pH of Pb^{2+} solutions used in isotherm experiments.
[b] In mg g^{-1}.
[c] In L mg^{-1}.
[d] std. dev of the fit.
[e] $L^{1/n}$ g^{-1} $mg^{1-1/n}$.
[f] ±std. dev.

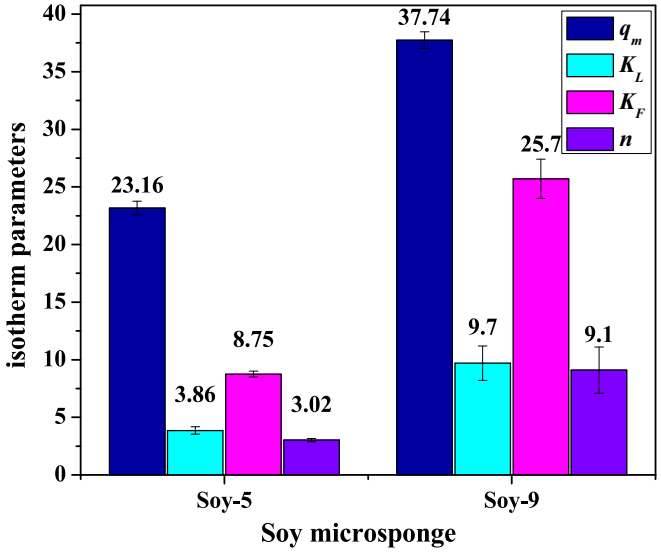

Fig. 8. Langmuir and Freundlich parameters values for the Pb^{2+} ion adsorption onto Soy-5 and Soy-9 microsponges from aqueous solutions containing $NaNO_3$ 0.1 mol L^{-1}, at pH = 5.0 and T = 298.15 K.

[30,77], by inverting the protein charge it is likely that the electrostatics interactions involved in β-structure stabilization are critically modified leading to aggregates disruption. This is also confirmed by the difficulties encountered during the voltammetric experiments carried out on metal ion solutions post adsorption. In fact, due to the release in solution of degradation products of soy proteins, at this pH value, a more accurate cleaning of electrodes was mandatory between measurements due to a particularly adhesiveness of substances released by the Soy 9 sample to the electrodes of the voltammetric cell.

A "regular" adsorption behavior was obtained at pH ≥ 5, i.e. above protein pI, as shown in Fig. SM4 b) and c). This indicates that Soy-9 sample can be regularly used for Pb^{2+} ions decontamination of wastewaters, the pH of which is not <5. The adsorption capacity of Soy-9 increases with the increase of pH (q_m = 37.74 and 56.2 mg g^{-1} at pH 5.0 and 6.5, respectively). Looking at the Pb^{2+} speciation profile obtained with literature formation constants of hydrolytic species in $NaClO_4$ (formation constants in this ionic medium can be compared to those in $NaNO_3$ considering that both are non-interacting media towards Pb^{2+}) [78,79], the formation percentage of Pb^{2+} aquo ion goes from 100 % to 95 % when the pH passes from 5.0 to 6.5. Considering that the remaining 5 % consists of the positively charged $Pb(OH)^+$ species, the increasing of q_m is not attributable to relevant changes in Pb^{2+} chemical speciation and can be explained as follow: i) at pH = 6.5, the competition between H^+ and Pb^{2+} ions for the binding sites of Soy-9 sample is lower; ii) at this pH, the binding sites of protein aggregate are almost deprotonated and, therefore, more available to bind the toxic metal ion.

Moreover, at pH = 5, i.e. close to the protein pI, electrostatic interactions are likely to be negligible while at pH = 6.5, i.e. above the pI, the electrostatic attraction between Pb^{2+} ions and the negatively charged microsponges surface may be a relevant factor leading to increased metal adsorption.

The ionic medium affects the adsorption capacity of Soy-9 sample and its effect depends on the type of ions coming from its dissociation. This assumption is confirmed by the q_m values obtained without ionic medium, in $NaNO_3$ 0.1 mol L^{-1} and in NaCl at the same ionic strength. The differences between the q_m values obtained at $I \rightarrow 0$ mol L^{-1} and in $NaNO_3$ 0.1 mol L^{-1} are within the experimental error (q_m = 36.40 and

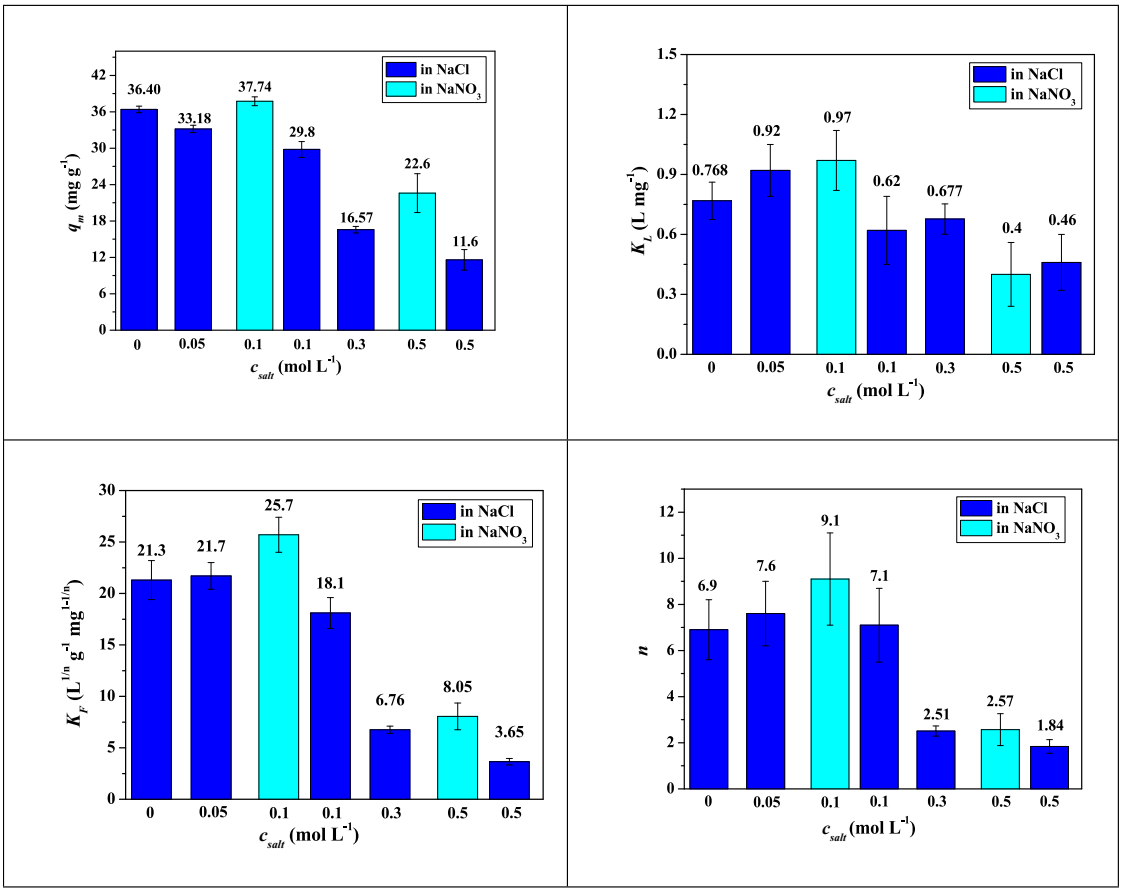

Fig. 9. Effect of ionic medium and of ionic strength on the Langmuir parameters q_m *(a) and* K_L (b) and on Freundlich parameters K_F (c) and n (d) for the Pb^{2+} ions adsorption onto Soy-9 sample. Other experimental details of metal ion solution: pH = 5.0, T = 298.15 K.

37.74 without ionic medium and in $NaNO_3$ 0.1 mol L^{-1}, respectively), while the addition of NaCl 0.1 mol L^{-1} reduces the adsorption capacity of the adsorbent by about 7 mg g^{-1}. Although the addition of $NaNO_3$ would appear to be irrelevant, a 5-fold increase of its concentration reduces the adsorption capacity of Soy-9 sample although the effect of $NaNO_3$ is always lower than that of NaCl (q_m = 22.6 and 11.6 mg g^{-1} at I = 0.5 mol L^{-1} in $NaNO_3$ and NaCl, respectively) (see histogram of Fig. 9 a)).

In Fig. SM6 a comparison is depicted between the sum of percentages of positively charged species of Pb^{2+} ions in solution (Σ+) and the q_m values of Soy-9 sample as function of ionic strength in NaCl and $NaClO_4$ or $NaNO_3$. The comparison of Σ+ and of q_m values provides useful information considering that the interaction between lead and the functional groups of the adsorbent mainly involves the positively charged species of the metal ion.

Independently of the ionic strength value, at pH = 5 and in $NaClO_4$, a non-interacting medium like $NaNO_3$, the Σ+ is 100 % like in absence of ionic medium ($I \rightarrow 0$ mol L^{-1}). This justifies the unvaried q_m value of Soy-9 sample with the addition of $NaNO_3$ 0.1 mol L^{-1} to the metal ion solution. Moreover, the reduction of q_m in $NaNO_3$ 0.5 mol L^{-1}, considering the unvaried Pb^{2+} speciation profile, can be explained in terms of competition of Na^+ ions towards binding sites of protein microsponges and/or in terms of shielding/shrinking effect on the microsponges caused by the ions of the more concentrated ionic medium and consequent reduction of available binding.

The gradual and higher q_m reduction observed with the increasing of NaCl concentration can be explained, as for $NaNO_3$, by competing and/or shielding effects of the ions coming from NaCl dissociation; in addition, a significant reduction of Σ+ (Σ+ = 100 and 49.7 % at pH = 5.0, at $I \rightarrow 0$ mol L^{-1} and in NaCl 0.5 mol L^{-1}, respectively) must be considered in the explanation.

The presence of ionic medium in the Pb^{2+} ions solution reduces also the affinity (K_L values) of the adsorbent material towards the target metal ion, but, unlike q_m, the effect of NaCl and $NaNO_3$, considering the experimental errors, is equivalent (K_L = 0.768, 0.40 and 0.46 L mg^{-1} without ionic medium, in $NaNO_3$ 0.5 mol L^{-1} and in NaCl 0.5 mol L^{-1}, respectively) (see histogram of Fig. 9 b)).

The results of adsorption isotherms reflect the trend of the ΔpH values, i.e. the mean difference between the pH at adsorption equilibrium and that of solution before adsorption ($pH_f - pH_i$) measured in each batch of each adsorption experiment (see Tables 2 and 3).

At pH_i = 5.0, in absence of background salt and in $NaNO_3$, the ΔpH is ~0.6, while, in NaCl it gradually increases with increasing of ionic strength going from 0.7 in NaCl 0.05 mol L^{-1} to 1.07 in NaCl 0.5 mol L^{-1}. The increase of solution pH at the end of the experiments is presumably due to the protonation of some functional groups of the protein aggregate. Indeed, at pH_i = 5.0, the H^+ ions of solution compete with the Pb^{2+} ions towards binding groups of the adsorbent material. The competition of H^+ ions is more significant in NaCl in which the formation of chloride species of Pb^{2+}, that gradually increases with the increase of NaCl concentration, reduces the percentage of positively charged species of the metal ion. At pH_i = 6.5 the H^+ competition is reduced and Pb^{2+} ions are adsorbed to the Soy-9 sample also replacing the proton of some protonated sites causing the pH reduction (ΔpH = −0.62).

In the last decade, the plethora of scientific articles concerning the adsorption of toxic metals from polluted waters has been enriched a number of works concerning the use of promising adsorbents based on or enriched with amyloid structures [14,25,42,58,80–83]. A selection of literature data regarding the Pb^{2+} ion adsorption onto amyloid protein

materials is collected in Table SM1 of Supplementary material. An example of hybrid material formed by protein amyloid fibrils of sunflower and peanut meals coupled with carbon membranes was proposed by Soon et al. in 2022 [80]. These materials removed efficiently heavy metals, including lead, from water solutions and their q_m values are of the same order of magnitude of those found for Soy-5 and Soy-9 microsponges presented in this work. Analogous considerations can be done for the q_m value found by Wu et al. [83] for the Pb^{2+} adsorption onto biofilms of BSA. Also Yang et al. [81] demonstrated the excellent Pb^{2+} sorption ability of a protein-based hybrid material formed by bovine serum albumin, tris(2-carboxyethyl) phosphine and sodium carboxymethyl cellulose (PTB/CMC) that has a $q_m = 105.4$ mg g^{-1} at pH = 6.5 and $T = 298.15$ K. However, in our previous work [25] we demonstrated that, despite the different experimental conditions, amyloid particulates based only on BSA can present comparable or better adsorption ability than hybrid materials. Furthermore, our data underline the fact that in addition to the metal ion binding sites, intrinsically present in the originating protein, the 3D structure of the BSA particulates [25] before and of Soy-5 and Soy-9 microsponges now, is crucial for the metal binding ability. Micro-FTIR measurements on Soy-9 micro sponges after Pb^{2+} ions adsorption are also reported in supporting information (Fig. SM7). In the sample containing Pb^{2+} ions a slight increase in the intermolecular β-structure is observed (the fractional area of the peak centred at 1621 cm^{-1} grows from 24 % to 27 %). This supports the hypothesis that intermolecular β-sheets are involved in metal uptake [25,84]. Importantly, the low cost and high abundance of SPI place it in the forefront as an excellent alternative biomaterial to the amyloid adsorbents already proposed.

3.6. Recycle and reuse of Soy-9 sample

The adsorbent recycling is a very important aspect of environmental decontamination processes. Indeed, the possibility of reusing the same material n times proportionally reduces the costs of the process. Thus, recycle and reuse experiments have been carried out with Soy-9 sample, the best adsorbent material towards Pb^{2+} ions, making four adsorption/desorption cycles (see Section 2.4 for experimental details). The results, in terms of q_e of adsorption and desorption of the four cycles are depicted in the histogram reported in Fig. 10.

The Soy-9 sample showed a good reuse capacity. In particular, in the first cycle the q_e of adsorption reach the 35.2 mg g^{-1}. In the next three

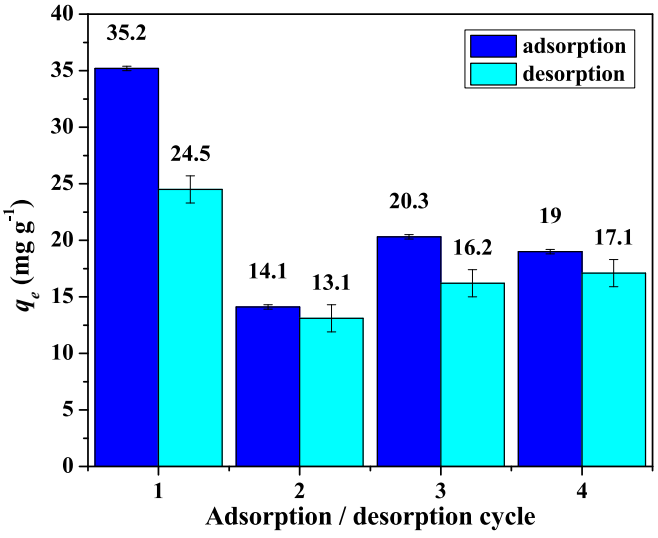

Fig. 10. q_e values of adsorption/desorption steps. Experimental details: amount of Soy-9 sample ≈5 mg; metal ion solution: 15 mL of Pb^{2+} ($c_{Pb2+} \approx 30$ mg L^{-1}), pH = 5.0, in $NaNO_3$ 0.1 mol L^{-1} and $T = 298.15$ K; extractant solution: 15 mL of EDTA 0.10 mol L^{-1}.

adsorption/desorption cycles the adsorption ability of the adsorbent decreases of ~40 % and, with some small fluctuation, remains almost constant.

The recovered metal ion in the first desorption step is lower than the adsorbed one ($q_{e\ adsorption} - q_{e\ desorption} = 10.7$ mg g^{-1}), while, starting from the second cycle, the amount of Pb^{2+} ion adsorbed and desorbed are comparable. This could be the reason of the lowering of adsorption ability of the adsorbent material after the first cycle. Indeed, part of the metal ion adsorbed in the first adsorption step is likely covalently bounded to the adsorbent and the EDTA solution is not able to extract it. Another explanation could be the partial degradation of Soy-9 sample during the reuse experiments.

4. Conclusions

We have presented a quantitative study on the successful production of highly efficient SPI-based microsponges for water purification application. The material is entirely composed of the plant-based SPI and is fabricated by a simple production procedure with minimal use of chemical reagents. This results in an environmentally-sustainable and low-cost platform, matching the basic principles of green chemistry. Following peculiarities of their molecular structures, micronscale protein aggregates exhibit different physico-chemical properties that can be suitably pre-set by tuning growing conditions.

SPI microsponges described in this work, successfully removed Pb^{2+} ions from aqueous environments, also demonstrating a high degree of recycling in terms of multiple use of the same composite matrix. Subtle variations of the production conditions translated into substantially different performance of the materials. Specifically, by simply changing the pH of the solution, from the isoelectric point (pH 5) to a pH where proteins are highly charged (pH 9), we obtained micron-sized aggregates with different content of intermolecular β-structures and internal polarity. They presented a certain ability in removing Pb^{2+} ions from water at pH values above protein isoelectric point (>pH 5), making these materials suitable for drinking and waste water purification.

The fact that the sample grown at pH 5 presented a lower affinity with respect to the one grown in solution at pH 9 allowed us to highlight general properties of protein aggregates, which may regulate metal sorption. We showed that specific interaction occurs between O—H of the carboxylic acids and C—N of the amino groups and cysteines for both samples. However, interestingly, Soy-5 sample, which has a lower affinity for Pb^{2+}, presents in the IR spectrum a supplementary fingerprint of a specific binding site (976 cm^{-1}) which may be attributed to specific electrostatic interactions with protein. In addition to the latter, also hydrophobic interactions and hydrogen bonding appeared to be significantly involved in metal binding. Furthermore, although both samples present intermolecular β-structures typical of amyloids, the sample with higher level of order and hydrophobicity is characterized by an enhanced metal binding affinity. This suggests that water molecules are important players in regulating the metal binding efficiency and in particular our data suggest that the binding efficiency is hindered in media with increased dielectric constant.

CRediT authorship contribution statement

Sara Anselmo: Investigation, Formal analysis, Methodology, Writing – review & editing, Data curation, Visualization. **Tiziana Avola:** Investigation, Formal analysis, Methodology, Data curation, Visualization. **Kleopatra Kalouta:** Investigation, Formal analysis, Methodology, Writing – review & editing, Data curation, Visualization. **Salvatore Cataldo:** Investigation, Data curation. **Giuseppe Sancataldo:** Investigation, Visualization, Writing – review & editing. **Nicola Muratore:** Investigation, Methodology, Data curation. **Vito Foderà:** Conceptualization, Supervision, Project administration, Funding acquisition, Writing – review & editing, Resources. **Valeria Vetri:** Conceptualization, Methodology, Validation, Investigation, Formal analysis,

Supervision, Writing – original draft, Writing – review & editing, Project administration, Funding acquisition, Resources. **Alberto Pettignano:** Methodology, Data curation, Validation, Investigation, Formal analysis, Supervision, Writing – original draft, Writing – review & editing.

Declaration of competing interest

The authors declare that they have no known competing financial interests or personal relationships that could have appeared to influence the work reported in this paper.

Acknowledgments

The authors thank the University of Palermo for financial support (FFR – PROMETA, FFR2021 and FFR2023). The VILLUM FONDEN (Villum Young Investigator Grant, project number: 19175) and the Novo Nordisk Foundation (NNF20OC00652) are also acknowledged for funding the project.

Appendix A. Supplementary data

Supplementary data to this article can be found online at https://doi.org/10.1016/j.ijbiomac.2023.124276.

References

[1] A.J. Mearns, D.J. Reish, P.S. Oshida, et al., Effects of pollution on marine organisms, Water Environ. Res. 86 (10) (2014) 1869–1954, https://doi.org/10.2175/106143014XI403l280668498.
[2] S. Bolisetty, M. Peydayesh, R. Mezzenga, Sustainable technologies for water purification from heavy metals: review and analysis, Chem. Soc. Rev. 48 (2) (2019) 463–487, https://doi.org/10.1039/C8CS00493E.
[3] W. Ahmad, R.D. Alharthy, M. Zubair, M. Ahmed, A. Hameed, S. Rafique, Toxic and heavy metals contamination assessment in soil and water to evaluate human health risk, Scientific Reports 11 (1) (2021) 1–12, https://doi.org/10.1038/s41598-021-94616-4.
[4] Transforming our world: the 2030 Agenda for Sustainable Development | Department of Economic and Social Affairs. Accessed August 2, 2022. https://sdgs.un.org/2030agenda.
[5] F.S.A. Khan, N.M. Mubarak, Y.H. Tan, et al., Magnetic nanoparticles incorporation into different substrates for dyes and heavy metals removal—a review, Environ. Sci. Pollut. Res. Int. 27 (35) (2020) 43526–43541, https://doi.org/10.1007/S11356-020-10482-Z.
[6] X. Liu, Research progress on treatment technology of produced water by adsorption method, IOP Conf Ser Mater Sci Eng 472 (1) (2019), https://doi.org/10.1088/1757-899X/472/1/012082.
[7] R. Wang, L. Deng, X. Fan, K. Li, H. Lu, W. Li, Removal of heavy metal ion cobalt (II) from wastewater via adsorption method using microcrystalline cellulose–magnesium hydroxide, Int. J. Biol. Macromol. 189 (2021) 607–617, https://doi.org/10.1016/j.ijbiomac.2021.08.156.
[8] Y. Fang, X. Lv, X. Xu, et al., Three-dimensional nanoporous starch-based material for fast and highly efficient removal of heavy metal ions from wastewater, Int. J. Biol. Macromol. 164 (2020) 415–426, https://doi.org/10.1016/j.ijbiomac.2020.07.017.
[9] F.S.A. Khan, N.M. Mubarak, Y.H. Tan, et al., A comprehensive review on magnetic carbon nanotubes and carbon nanotube-based buckypaper for removal of heavy metals and dyes, J. Hazard. Mater. (2021) 413, https://doi.org/10.1016/j.jhazmat.2021.125375.
[10] H.A. Aziz, M.N. Adlan, K.S. Ariffin, Heavy metals (Cd, pb, zn, ni, cu and Cr(III)) removal from water in Malaysia: post treatment by high quality limestone, Bioresour. Technol. 99 (6) (2008) 1578–1583, https://doi.org/10.1016/j.biortech.2007.04.007.
[11] A. Nalaparaju, J. Jiang, Ion exchange in metal-organic framework for water purification: insight from molecular simulation, J. Phys. Chem. C 116 (12) (2012) 6925–6931, https://doi.org/10.1021/JP210082F.
[12] L. Zhang, Y. Wu, X. Qu, Z. Li, J. Ni, Mechanism of combination membrane and electro-winning process on treatment and remediation of Cu2+polluted water body, J. Environ. Sci. 21 (6) (2009) 764–769, https://doi.org/10.1016/S1001-0742(08)62338-4.
[13] A. Ahmadi, T. Wu, Towards full cell potential utilization during water purification using Co/Bi/TiO2 nanotube electrodes, Electrochim. Acta 364 (2020), 137272, https://doi.org/10.1016/j.electacta.2020.137272.
[14] D. Liu, Z. Li, W. Li, et al., Adsorption behavior of heavy metal ions from aqueous solution by soy protein hollow microspheres, Ind. Eng. Chem. Res. 52 (32) (2013) 11036–11044, https://doi.org/10.1021/ie401092f.
[15] J. Qu, Research progress of novel adsorption processes in water purification: a review, J. Environ. Sci. 20 (1) (2008) 1–13, https://doi.org/10.1016/S1001-0742(08)60001-7.
[16] S.R. Popuri, Y. Vijaya, V.M. Boddu, K. Abburi, Adsorptive removal of copper and nickel ions from water using chitosan coated PVC beads, Bioresour. Technol. 100 (1) (2009) 194–199, https://doi.org/10.1016/j.biortech.2008.05.041.
[17] X. Xu, R. Hao, H. Xu, A. Lu, Removal mechanism of Pb(II) by Penicillium polonicum: immobilization, adsorption, and bioaccumulation, Scientific Reports 10 (1) (2020) 1–12, https://doi.org/10.1038/s41598-020-66025-6.
[18] H. Demey, T. Vincent, E. Guibal, A novel algal-based sorbent for heavy metal removal, Chem. Eng. J. 332 (2018) 582–595, https://doi.org/10.1016/j.cej.2017.09.083.
[19] T. Halttunen, S. Salminen, R. Tahvonen, Rapid removal of lead and cadmium from water by specific lactic acid bacteria, Int. J. Food Microbiol. 114 (1) (2007) 30–35, https://doi.org/10.1016/j.ijfoodmicro.2006.10.040.
[20] M. Bansal, U. Garg, D. Singh, V.K. Garg, Removal of Cr(VI) from aqueous solutions using pre-consumer processing agricultural waste: a case study of rice husk, J. Hazard. Mater. 162 (1) (2009) 312–320, https://doi.org/10.1016/j.jhazmat.2008.05.037.
[21] A.A. Atia, A.M. Donia, S.A. Abou-El-Enein, A.M. Yousif, Studies on uptake behaviour of copper(II) and lead(II) by amine chelating resins with different textural properties, Sep. Purif. Technol. 33 (3) (2003) 295–301, https://doi.org/10.1016/S1383-5866(03)00089-3.
[22] M. Nasrollahzadeh, M. Sajjadi, S. Iravani, R.S. Varma, Starch, cellulose, pectin, gum, alginate, chitin and chitosan derived (nano)materials for sustainable water treatment: a review, Carbohydr. Polym. 251 (2021), 116986, https://doi.org/10.1016/j.carbpol.2020.116986.
[23] S. Cataldo, A. Gianguzza, A. Pettignano, I. Villaescusa, Mercury(II) removal from aqueous solution by sorption onto alginate, pectate and polygalacturonate calcium gel beads. A kinetic and speciation based equilibrium study, React. Funct. Polym. 73 (1) (2013) 207–217, https://doi.org/10.1016/j.reactfunctpolym.2012.10.005.
[24] S. Cataldo, A. Gianguzza, A. Pettignano, Sorption of Pd(II) ion by calcium alginate gel beads at different chloride concentrations and pH. A kinetic and equilibrium study, Arab. J. Chem. 9 (5) (2016) 656–667, https://doi.org/10.1016/j.arabjc.2014.10.031.
[25] S. Anselmo, S. Cataldo, T. Avola, et al., Lead(II) ions adsorption onto amyloid particulates: an in depth study, J. Colloid Interface Sci. 610 (2022) 347–358, https://doi.org/10.1016/j.jcis.2021.11.184.
[26] S. Bolisetty, R. Mezzenga, Amyloid–carbon hybrid membranes for universal water purification, Nat. Nanotechnol. 11 (4) (2016) 365–371, https://doi.org/10.1038/nnano.2015.310.
[27] M. Vandenbossche, M. Jimenez, M. Casetta, M. Traisnel, Remediation of heavy metals by biomolecules: a review, Crit. Rev. Environ. Sci. Technol. 45 (15) (2015) 1644–1704, https://doi.org/10.1080/10643389.2014.966425.
[28] Y. Shen, A. Levin, A. Kamada, et al., From protein building blocks to functional materials, ACS Nano 15 (4) (2021) 5819–5837, https://doi.org/10.1021/acsnano.0c08510.
[29] V. Vetri, F. Piccirilli, J. Krausser, et al., Ethanol controls the self-assembly and mesoscopic properties of human insulin amyloid spherulites, J. Phys. Chem. B 122 (12) (2018) 3101–3112, https://doi.org/10.1021/acs.jpcb.8b01779.
[30] M.G. Santangelo, V. Foderà, V. Militello, V. Vetri, Back to the oligomeric state: pH-induced dissolution of concanavalin a amyloid-like fibrils into non-native oligomers, RSC Adv. 6 (79) (2016) 75082–75091, https://doi.org/10.1039/C6RA16690C.
[31] S. Anselmo, G. Sancataldo, V. Foderà, V. Vetri, α-casein micelles-membranes interaction: flower-like lipid protein coaggregates formation, Biochim. Biophys. Acta, Gen. Subj. 1866 (10) (2022), 130196, https://doi.org/10.1016/j.bbagen.2022.130196.
[32] D. Fennema Galparsoro, X. Zhou, A. Jaaloul, F. Piccirilli, V. Vetri, V. Foderà, Conformational transitions upon maturation rule surface and pH-responsiveness of α-lactalbumin microparticulates, ACS Appl. Bio Mater. 4 (2) (2021) 1876–1887, https://doi.org/10.1021/acsabm.0c01541.
[33] S. Bolisetty, N. Reinhold, C. Zeder, M.N. Orozco, R. Mezzenga, Efficient purification of arsenic-contaminated water using amyloid–carbon hybrid membranes, Chem. Commun. 53 (42) (2017) 5714–5717, https://doi.org/10.1039/C7CC00406K.
[34] Q. Zhang, S. Bolisetty, Y. Cao, et al., Selective and efficient removal of fluoride from water: in situ engineered amyloid fibril/ZrO2 hybrid membranes, Angew Chem-Int Edit. 58 (18) (2019) 6012–6016, https://doi.org/10.1002/anie.201901596.
[35] M. Peydayesh, M.K. Suter, S. Bolisetty, et al., Amyloid fibrils aerogel for sustainable removal of organic contaminants from water, Adv. Mater. 32 (12) (2020) 1907932, https://doi.org/10.1002/adma.201907932.
[36] P. Singh, R. Kumar, S.N. Sabapathy, A.S. Bawa, Functional and edible uses of soy protein products, Compr. Rev. Food Sci. Food Saf. 7 (1) (2008) 14–28, https://doi.org/10.1111/J.1541-4337.2007.00025.X.
[37] F. Song, D.L. Tang, X.L. Wang, Y.Z. Wang, Biodegradable soy protein isolate-based materials: a review, Biomacromolecules 12 (10) (2011) 3369–3380, https://doi.org/10.1021/bm200904x.
[38] M.B. Stie, K. Kalouta, C.F.B. da Cunha, H.M. Feroze, V. Vetri, V. Foderà, Sustainable strategies for waterborne electrospinning of biocompatible nanofibers based on soy protein isolate, Sustain. Mater. Technol. 34 (2022), e00519, https://doi.org/10.1016/j.susmat.2022.e00519.
[39] D. Fukushima, Soy proteins, in: Handbook of Food Proteins, 2011, pp. 210–232, https://doi.org/10.1533/9780857093639.210. Published online.
[40] D.P. Jaramillo, R.F. Roberts, J.N. Coupland, Effect of pH on the properties of soy protein–pectin complexes, Food Res. Int. 44 (4) (2011) 911–916, https://doi.org/10.1016/j.foodres.2011.01.057.

[41] E. Álvarez-Castillo, J.M. Aguilar, C. Bengoechea, M.L. López-Castejón, A. Guerrero, Rheology and water absorption properties of alginate-soy protein composites, Polymers (Basel) 13 (11) (2021) 1807, https://doi.org/10.3390/polym13111807.
[42] J. Liu, D. Su, J. Yao, Y. Huang, Z. Shao, X. Chen, Soy protein-based polyethylenimine hydrogel and its high selectivity for copper ion removal in wastewater treatment, J. Mater. Chem. A Mater. 5 (8) (2017) 4163–4171, https://doi.org/10.1039/C6TA10814H.
[43] V. Vetri, V. Foderà, The route to protein aggregate superstructures: particulates and amyloid-like spherulites, FEBS Lett. 589 (9PartA) (2015) 2448–2463, https://doi.org/10.1016/j.febslet.2015.07.006.
[44] C. Stringari, A. Cinquin, O. Cinquin, M.A. Digman, P.J. Donovan, E. Gratton, Phasor approach to fluorescence lifetime microscopy distinguishes different metabolic states of germ cells in a live tissue, Proc. Natl. Acad. Sci. 108 (33) (2011) 13582–13587, https://doi.org/10.1073/pnas.1108161108.
[45] Data Tables | Fluorescence Lifetime Standards | ISS. Accessed August 2, 2022. https://iss.com/resources/reference/data_tables/FL_LifetimeStandards.html.
[46] Fluorescence quantum yields (QY) and lifetimes (τ) for Alexa Fluor dyes—Table 1.5 | Thermo Fisher Scientific - IT. Accessed August 2, 2022. https://www.thermofisher.com/it/en/home/references/molecular-probes-the-handbook/tables/fluorescence-quantum-yields-and-lifetimes-for-alexa-fluor-dyes.html.
[47] S. Lagergren, About the theory of so-called adsorption of soluble substances 24 (6) (1898) 1–39.
[48] U. Wingenfelder, C. Hansen, G. Furrer, R. Schulin, Removal of heavy metals from mine waters by natural zeolites, Environ. Sci. Technol. 39 (2005) 4606–4613, https://doi.org/10.1021/es048482s.
[49] K.L. Tan, B.H. Hameed, Insight into the adsorption kinetics models for the removal of contaminants from aqueous solutions, J. Taiwan Inst. Chem. Eng. 74 (2017) 25–48, https://doi.org/10.1016/j.jtice.2017.01.024.
[50] H. Freundlich, Über die adsorption in Lösungen, Z. Phys Chem. 57U (1) (1907) 385–470.
[51] I. Langmuir, The adsorption of gases on plane surfaces of glass, mica and platinum, J. Am. Chem. Soc. 40 (9) (1918) 1361–1403.
[52] S. Zölls, M. Gregoritza, R. Tantipolphan, et al., How subvisible particles become invisible-relevance of the refractive index for protein particle analysis, J. Pharm. Sci. 102 (5) (2013) 1434–1446, https://doi.org/10.1002/jps.23479.
[53] F. Piccirilli, G. Schirò, V. Vetri, S. Lupi, A. Perucchi, V. Militello, Decoding vibrational states of concanavalin a amyloid fibrils, Biophys. Chem. 199 (2015) 17–24, https://doi.org/10.1016/j.bpc.2015.02.007.
[54] H. Fabian, W. Mantele, Infrared Spectroscopy of Proteins. Handbook of Vibrational Spectroscopy, 2006, https://doi.org/10.1002/0470027320.S8201. Published online August 15.
[55] Sitnikova Usoltsev, Uspenskaya Kajava, Systematic FTIR spectroscopy study of the secondary structure changes in human serum albumin under various denaturation conditions, Biomolecules 9 (8) (2019) 359, https://doi.org/10.3390/biom9080359.
[56] M. Jackson, H.H. Mantsch, Protein secondary structure from FT-IR spectroscopy: correlation with dihedral angles from three-dimensional ramachandran plots, Can. J. Chem. 69 (11) (2011) 1639–1642, https://doi.org/10.1139/V91-240.
[57] C. Wang, L. Jiang, D. Wei, et al., Effect of secondary structure determined by FTIR spectra on surface hydrophobicity of soybean protein isolate, Procedia Eng. 15 (2011) 4819–4827, https://doi.org/10.1016/j.proeng.2011.08.900.
[58] M. Peydayesh, S. Bolisetty, T. Mohammadi, R. Mezzenga, Assessing the binding performance of amyloid-carbon membranes toward heavy metal ions, Langmuir 35 (11) (2019) 4161–4170, https://doi.org/10.1021/acs.langmuir.8b04234.
[59] V. Foderà, M. Groenning, V. Vetri, et al., Thioflavin T hydroxylation at basic pH and its effect on amyloid fibril detection, J. Phys. Chem. B 112 (47) (2008) 15174–15181, https://doi.org/10.1021/jp805560c.
[60] M.G. di Carlo, V. Minicozzi, V. Foderà, et al., Thioflavin T templates amyloid β(1–40) conformation and aggregation pathway, Biophys. Chem. 206 (2015) 1–11, https://doi.org/10.1016/J.BPC.2015.06.006.
[61] D.J. Lindberg, M.S. Wranne, M. Gilbert Gatty, F. Westerlund, E.K. Esbjörner, Steady-state and time-resolved thioflavin-T fluorescence can report on morphological differences in amyloid fibrils formed by Aβ(1–40) and Aβ(1–42), Biochem. Biophys. Res. Commun. 458 (2) (2015) 418–423, https://doi.org/10.1016/j.bbrc.2015.01.132.
[62] G. de Luca, D. Fennema Galparsoro, G. Sancataldo, M. Leone, V. Foderà, V. Vetri, Probing ensemble polymorphism and single aggregate structural heterogeneity in insulin amyloid self-assembly, J. Colloid Interface Sci. 574 (2020) 229–240, https://doi.org/10.1016/J.JCIS.2020.03.107.
[63] M.A. Morando, F. Venturella, M. Sollazzo, et al., Solution structure of recombinant pvfp-5β reveals insights into mussel adhesion, Commun. Biol. 5 (1) (2022) 1–10, https://doi.org/10.1038/s42003-022-03699-w.
[64] D.L. Sackett, J. Wolff, Nile red as a polarity-sensitive fluorescent probe of hydrophobic protein surfaces, Anal. Biochem. 167 (2) (1987) 228–234, https://doi.org/10.1016/0003-2697(87)90157-6.
[65] J.A. Levitt, P.H. Chung, K. Suhling, Spectrally resolved fluorescence lifetime imaging of Nile red for measurements of intracellular polarity, J. Biomed. Opt. 20 (9) (2015), 096002, https://doi.org/10.1117/1.JBO.20.9.096002.
[66] S. Barber-Zucker, B. Shaanan, R. Zarivach, Transition metal binding selectivity in proteins and its correlation with the phylogenomic classification of the cation diffusion facilitator protein family, Sci. Rep. 7 (1) (2017) 1–12, https://doi.org/10.1038/s41598-017-16777-5.
[67] J.D. Cox, J.A. Hunt, K.M. Compher, C.A. Fierke, D.W. Christianson, Structural influence of hydrophobic core residues on metal binding and specificity in carbonic anhydrase II, Biochemistry 39 (45) (2000) 13687–13694, https://doi.org/10.1021/BI001649J.
[68] Chen Q. Yu, L. Yang, L. Liu, et al., Combined forms of Pb and its detoxification and absorption in Cladophora rupestris subcells, Spectrochim. Acta A Mol. Biomol. Spectrosc. 248 (2021), 119190, https://doi.org/10.1016/j.saa.2020.119190.
[69] G. Guibaud, N. Tixier, A. Bouju, M. Baudu, Relation between extracellular polymers' composition and its ability to complex Cd, Cu and Pb, Chemosphere 52 (10) (2003) 1701–1710, https://doi.org/10.1016/S0045-6535(03)00355-2.
[70] R.G. Huamani-Palomino, C.R. Jacinto, H. Alarcón, et al., Chemical modification of alginate with cysteine and its application for the removal of Pb(II) from aqueous solutions, Int. J. Biol. Macromol. 129 (2019) 1056–1068, https://doi.org/10.1016/j.ijbiomac.2018.09.096.
[71] S. Cazalbou, G. Bertrand, C. Drouet, Tetracycline-loaded biomimetic apatite: an adsorption study, J. Phys. Chem. B 119 (7) (2015) 3014–3024, https://doi.org/10.1021/JP5116756.
[72] D. Ouyang, Y. Zhuo, L. Hu, Q. Zeng, Y. Hu, Z. He, Research on the adsorption behavior of heavy metal ions by porous material prepared with silicate tailings, Minerals 9 (5) (2019) 291, https://doi.org/10.3390/min9050291.
[73] S. Cataldo, P. Lo Meo, P. Conte, A. di Vincenzo, D. Milea, A. Pettignano, Evaluation of adsorption ability of cyclodextrin-calixarene nanosponges towards Pb2+ ion in aqueous solution, Carbohydr Polym. 267 (2021), 118151, https://doi.org/10.1016/j.carbpol.2021.118151.
[74] Z. Zhang, S. He, Y. Zhang, et al., Spectroscopic investigation of Cu2+, Pb2+ and Cd2+ adsorption behaviors by chitosan-coated argillaceous limestone: competition and mechanisms, Environ. Pollut. 254 (2019), 112938, https://doi.org/10.1016/j.envpol.2019.07.106.
[75] L. Liu, Y. Huang, Y. Meng, et al., Investigating the adsorption behavior and quantitative contribution of Pb2+ adsorption mechanisms on biochars by different feedstocks from a fluidized bed pyrolysis system, Environ. Res. 187 (2020), 109609, https://doi.org/10.1016/j.envres.2020.109609.
[76] S. He, Y. Li, L. Weng, et al., Competitive adsorption of Cd2+, Pb2+ and Ni2+ onto Fe3+-modified argillaceous limestone: influence of pH, ionic strength and natural organic matters, Sci. Total Environ. 637–638 (2018) 69–78, https://doi.org/10.1016/j.scitotenv.2018.04.300.
[77] X. Zhou, D. Fennema Galparsoro, A. Østergaard Madsen, et al., Polysorbate 80 controls morphology, structure and stability of human insulin amyloid-like spherulites, J. Colloid Interface Sci. 606 (2022) 1928–1939, https://doi.org/10.1016/j.jcis.2021.09.132.
[78] C.F. Baes, R.E. Mesmer, The Hydrolysis of Cations, John Wiley & Sons, 1976.
[79] S. Cataldo, G. Lando, D. Milea, S. Orecchio, A. Pettignano, S. Sammartano, A novel thermodynamic approach for the complexation study of toxic metal cations by a landfill leachate, New J. Chem. 42 (10) (2018) 7640–7648, https://doi.org/10.1039/C7NJ04456A.
[80] W.L. Soon, M. Peydayesh, R. Mezzenga, A. Miserez, Plant-based amyloids from food waste for removal of heavy metals from contaminated water, Chem. Eng. J. 445 (2022), 136513, https://doi.org/10.1016/j.cej.2022.136513.
[81] F. Yang, Q. Yang, M. Chen, C. Luo, W. Chen, P. Yang, Toxic metal ion sequestration by amyloid-mediated fast coacervation, Cell Rep. Phys. Sci. 2 (3) (2021), 100379, https://doi.org/10.1016/j.xcrp.2021.100379.
[82] M. Peydayesh, R. Mezzenga, Protein nanofibrils for next generation sustainable water purification, Nat. Commun. 12 (1) (2021) 1–17, https://doi.org/10.1038/S41467-021-23388-2.
[83] X. Wu, X. Han, L. Lv, M. Li, J. You, C. Li, Supramolecular proteinaceous biofilms as trapping sponges for biologic water treatment and durable catalysis, J. Colloid Interface Sci. 527 (2018) 117–123, https://doi.org/10.1016/j.jcis.2018.05.036.
[84] M. Peydayesh, M. Bagnani, W.L. Soon, R. Mezzenga, Turning food protein waste into sustainable technologies, Chem. Rev. 123 (5) (2023) 2112–2154, https://doi.org/10.1021/acs.chemrev.2c00236.